THE FLORIDA STATE UNIVERSITY

COLLEGE OF ARTS AND SCIENCES

# AN INTERCOMPARISON OF NUMERICALLY MODELED FLUX DATA AND SATELLITE-DERIVED FLUX DATA FOR WARM SECLUSIONS

By

JOEL PAUL SCOTT

A thesis submitted to the
Department of Earth, Ocean and Atmospheric Science
in partial fulfillment of the
requirements for the degree of
Master of Science

Degree Awarded:
Summer Semester, 2011

The members of the committee approve the thesis of Joel P. Scott defended on March 29, 2011.

_____
Mark A. Bourassa
Professor Directing Thesis

_____
Carol Anne Clayson
Professor Co-Directing Thesis

_____
Philip Sura
Committee Member

The Graduate School has verified and approved the above-named committee members.

Dedicated to those who have inspired me to pursue my dreams, to follow my heart, and to be true to myself…

# ACKNOWLEDGEMENTS

The funding for this research was provided through NASA NEWS and NOAA COD. I would like to thank my major and co-major professors, Dr. Mark Bourassa and Dr. Carol Anne Clayson, for their direction, guidance, and support as well as the opportunity to seek a Master's degree. I would also like to thank Dr. Sura for serving on my committee. I thank Paul Hughes for his work on the flux look-up tables, Alec Bogdanoff for his assistance with the SeaFlux data set, and Ryan Maue for his warm seclusion identification algorithm. I also thank Kathy Fearon for her direction and guidance while writing my thesis. Additionally, I thank my labmates and friends, for their support, humor, and encouragement through my research and writing.

# TABLE OF CONTENTS

# LIST OF TABLES

# LIST OF FIGURES

# ABSTRACT

Warm seclusions are large midlatitude storms that have the potential to substantially influence the turbulent heat fluxes and global energy budget. These storms have not been previously investigated from an energy and flux perspective. They have large areas of strong surface winds and rapidly moving cold fronts, which are associated with large air-sea differences of temperature and humidity. These regions contain large air-sea fluxes of latent and sensible heat. Therefore, errors in model representation of warm seclusions may introduce significant bias and uncertainty to the energy budget. The turbulent heat fluxes associated with three specific warm seclusions in different ocean basins are examined through an intercomparison of satellite-derived flux data and numerically derived flux data. The satellite data includes the SeaFlux version 0.75 data derived from SSM/I (Special Sensor Microwave/Imager), and model-derived reanalysis data includes CFSR, ERA-Interim, MERRA, and NCEP-R2 reanalysis data sets. Latent and sensible heat fluxes are computed in a physically consistent manner though the use of a bulk flux parameterization A single warm seclusion, which typically lasts between three and seven days, is responsible for approximately one quarter of the total time-integrated monthly fluxes for the ocean basin containing the warm seclusion, depending on the storm and data set under consideration. The large area of extremely large fluxes is associated with the mature phase of the cyclone. Proper representation of these fluxes is critical to determining accurate monthly-averaged, basin-wide fluxes.

# CHAPTER ONE

# INTRODUCTION

Turbulent heat and energy fluxes play a critical role in the global energy budget and are key to understanding processes such as climate change, ice sheet evolution, and synoptic storm processes [*Bourassa et al.,* 2010a; *Bourassa et al.,* 2010b]. Multiple flux observation techniques exist, but for obtaining fluxes over the global oceans, where in situ measurements are sparse, satellite retrievals are advantageous [*Roberts et al.,* 2010]. Satellite-derived fluxes offer denser and broader spatial sampling compared to fluxes derived from the in situ ocean-observing network, which includes ships, buoys, and ocean profiling floats. Modern satellite-derived data have accuracies that are similar to the accuracies associated with in situ observations [*Bourassa et al.,* 2010a; *Jackson et al.,* 2009; *Roberts et al.,* 2010].

Increased spatial coverage offered by satellite observations, compared to the coverage of direct in situ measurements, reduces the impact of random errors and under sampling errors on the associated fluxes. Combining high-resolution data with the modern retrieval and regression techniques of *Jackson et al.* [2009] and *Roberts et al*. [2010] can reduce biases associated with the latent heat flux (LHF), the sensible heat flux (SHF), and the global energy budget. Better resolving the LHF and SHF will increase our knowledge and understanding of the global energy budget, enabling more accurate studies of weather events and climate [*Kent and Taylor,* 1995].

Satellite-derived fluxes are intercompared with numerically derived fluxes from several modern reanalysis products, resulting in a preliminary evaluation of the benefits of modern satellite retrieval techniques, with the secondary goal of improving the current understanding of the influence of large midlatitude storms on the global energy budget. Selected reanalyses are the Climate Forecast System Reanalysis (CFSR) [*Saha et al.,* 2010], the European Centre for Medium-Range Weather Forecasts (ECMWF) Re-Analysis Interim (ERA-Interim) [*Simmons et al.,* 2007], the Modern Era Retrospective-Analysis for Research and Applications (MERRA) [*Bosilovich et al.,* 2009], and the National Centers for Environmental Prediction–Department of Energy Atmospheric Model Intercomparison Project II Reanalysis (NCEP-DOE AMIP-II Reanalysis, also known as NCEP-R2) [*Kanamitsu et al.,* 2002]. This intercomparison uses a modularized flux testbed (MFT) to compute the fluxes (section 3.1). Rather than use the fluxes provided by these analyses, which do not always represent snapshots near the time of the satellite

overpass, and are not necessarily tuned to provide the most accurate fluxes (fluxes are calculated with a single bulk algorithm, section 3.1). This intercomparison is applied to large midlatitude storms, known as warm seclusions. These large cyclones are accompanied by hurricane force winds and occur frequently in the winter hemisphere. Their impact on the turbulent heat fluxes and their contribution to the global energy budget is not well known [*Maue*, 2010]. However, storms of this strength and spatial magnitude are generally associated with enormous fluxes and can have a significant impact on local and global energy budgets. These cyclones have been shown to have a considerable impact on hemispheric predictability according to multiple studies [*Anwender et al.*, 2008; *Harr and Dea*, 2009].

It is the purpose of this study to compute the air-sea fluxes and determine the impact of warm seclusions on regional energy budgets. Specifically, this study applies modern satellite retrieval and flux computation techniques as an indicator of the rough accuracy in the gridded products used. The storm-related fluxes in the gridded products are then used to establish the significance of warm seclusions to regional energy budgets. This type of analysis has not been conducted previously for warm seclusions and is important for determining the effect these storms have on the turbulent heat fluxes. Accounting for the effect of warm seclusions on these fluxes is important to reducing the associated biases and to improving climate studies and predictions.

# CHAPTER TWO

# BACKGROUND

A flux is the transfer rate of a quantity per unit area, and the concept of a flux can be applied to heat, momentum, mass, energy, or other physical quantities. Turbulent energy and moisture fluxes are the focus of this study. One such energy flux is the latent heat flux (LHF), which describes the transfer of heat energy per unit area associated with the change of phase for water. The other energy flux under consideration is the sensible heat flux (SHF), which relates the transfer of energy per unit area associated with a temperature change. Both SHF and LHF are given in units of watts per square meter, where a watt is the energy exchange per unit time. These fluxes and describe the transfer of energy from the ocean to the atmosphere and vice versa.

The LHF is closely related to a moisture flux, specifically, the evaporative flux. The evaporative flux is commonly given in millimeters of water evaporated per day. Therefore, the similarity can be seen between these two quantities, both involving the phase change of water. The LHF and the evaporative flux are related by a scaling factor known as the latent heat of vaporization, the energy required to evaporate a unit mass of water. Since these quantities are closely related, this study takes into consideration turbulent energy and moisture fluxes.

## 2.1 Flux estimations

Bulk methods are used to estimate surface turbulent energy fluxes. Fluxes are typically estimated from variables that are commonly observed and available from numerical models: wind, pressure, sea surface temperature, air temperature, and humidity. These variables must be known, or estimated, to apply this technique. The advantages of using satellite data to determine the input variables for bulk methods are broad spatial coverage and a small number of observing platforms to be considered for calibration and data regression techniques.

Historically, it has been difficult to determine atmospheric temperature and humidity close to the ocean surface from satellites [*Schlüssel et al*., 1995; *Schulz et al*., 1993; *Bentamy et al*. 2003]; bulk algorithms are typically calibrated to temperatures and moistures from a height of 2m or 10m above the local mean ocean surface. Recently, several regression techniques have stood out as useful in deriving the necessary quantities needed for flux computation from satellite

observations. *Jackson et al.,* [2009] and *Roberts et al.,* [2010] recently conducted research to improve satellite regression techniques. *Jackson et al.* [2009] implemented a multiple linear regression approach to derive the air temperature and the specific humidity. More recently, *Roberts et al*. [2010] applied a neural network methodology to derive these quantities from the satellite observations. A scatterplot comparison with in situ-based values from height-adjusted ICOADS (International Comprehensive Ocean-Atmosphere Data Set) for both methods of deriving air temperature and specific humidity is shown in Figures 2-1 and 2-2, respectively. These figures show that for most values of air temperature and specific humidity, both the neural network and linear regression techniques achieve fairly accurate results with respect to the ICOADS data [*Bourassa et al.,* 2010a]. Biases are steady over most of the parameter range, and random errors in these techniques are roughly 1.5 times the random error in buoy observations.

## 2.2 Biases and accuracy requirements

Biases and random errors negatively impact the accuracy of the turbulent heat fluxes, but these accuracies have varying relevance depending on the latitude and process under consideration. For example, biases on the order of 10 $Wm^{-2}$ in the LHF have significance in the tropics for processes that occur on an annual scale [*Weller et al.,* 2004; *Bourassa et al.,* 2010b], whereas biases on this same order are significant on seasonal time scales in the midlatitudes, where the mixed layer is relatively thin. Additionally, to produce results with significance for processes that occur over decades or centuries, such as would be useful in climate studies, the biases associated with the heat fluxes should be less than 1 $Wm^{-2}$ [*Hansen et al.*, 2005; *Johnson et al.*, 2007; *Levitus et al.*, 2009; *Bourassa et al.,* 2010b]. Table 2-1 and Figure 2-3 provide more detail of energy flux accuracy requirements for specific processes that occur on given temporal and spatial scales. To reduce bias and increase accuracy, modern retrieval techniques (Roberts et al. 2010), bias correction based on 2-1 and 2-2, and advanced flux computation algorithms (section 3.1) are applied to storms, specifically warm seclusions, in this study.

## 2.3 Warm seclusions

Warm seclusion extratropical cyclones are synoptic-scale midlatitude storm systems. Warm seclusions are a possible outcome of the extratropical transition of a tropical cyclone and occur during the mature stage in the lifecycle of an extratropical cyclone [*Bjerknes and Solberg,* 1922; *Shapiro and Keyser,* 1990]. During this stage, the storm system may be experiencing

either intensification or weakening [*Sanders and Gyakum,* 1980] on the basis of latent heat release (from condensation) associated with dynamic nonlinear feedbacks [*Maue,* 2010; *Raymond,* 1992; *Hart et al*., 2006]. These feedbacks may lead to substantial changes in dynamic structure of the storm in relatively short periods of time [*Rossa et al*., 2000]. Therefore, the energy flux interactions associated with these storms are an integral part of their formation, existence, and evolution. However, many questions remain unanswered regarding specific dynamic interactions of warm seclusions, including the mechanisms responsible for the formation and intensity of the high lower-tropospheric winds to the rear of the storm behind the bent-back warm front and seclusion [*Maue*, 2010]. The winds associated with this part of the storm are referred to as the dry intrusion occurring from the rear (Figure 2-4).

Warm seclusions are characterized by typical cyclonic thermodynamic structure. They have a warm core with calm air in the central "eye," surrounded by strong winds and clouds associated with the cold frontal systems (Figure 2-5) [*Maue,* 2010]. Warm seclusions may occupy a large spatial region, beginning as a relatively small disturbance along frontal boundaries but quickly evolving into a much larger feature (Figure 2-6).

The structure of warm seclusions differs from typical cyclonic structure in that a seclusion has a warm front occluded between two cold frontal systems (Figure 2-4). This basic structure may be thought of as a cold front followed, at some distance, by a warm air mass. A second, quickly moving cold front overtakes the warm, moist air, trapping it between the cold air masses and secluding it upward. This type of structure is known as the Shapiro-Keyser cyclone model [*Shapiro and Keyser*, 1990], which describes a zonally oriented system with a strong warm front and relatively weak leading cold front. This cyclone model is known for its comma-shaped cloud region (also termed T-bone structure or bent-back region) [*Neiman and Shapiro*, 1993]. The cloudy part of this structure is associated with the trailing cold front, in the lower flank of the cyclone bending to the rear of the storm, whereas the clear region just ahead of the comma-shape is the bent-back warm front [*Neiman and Shapiro*, 1993]. This T-bone feature is visible in satellite cloud and water vapor imagery, as well as in potential temperature (Figure 2-6). This structure has been termed a "triple point" by Maue [2010] and can be thought of as the intersection of the east-west oriented warm front and the north-south oriented cold front, with the bent-back warm front extending equatorward and to the rear of the storm, relative to the polar airstream.

The trailing cold front located behind the bent-back warm front is associated with the dry intrusion where air is descending adiabatically, warming and drying [*Browning,* 2004; *Parton et al.*, 2009; *Browning*, 1997]. This region contains hurricane force winds and houses cold, dry air, creating large air-sea gradients [*Shapiro and Keyser*, 1990; *Reed and Danielsen*, 1959]. These winds and air-sea differences exert a considerable influence on the LHF and SHF. Therefore, this region behind the trailing cold front is where the highest turbulent heat fluxes are expected to occur.

Regions of lower turbulent heat fluxes are anticipated in the regions containing the primary and secondary warm conveyor belts (WCB), depicted in Figure 2-4. These conveyor belts obey the quasi-Lagrangian conveyor belt model of Harrold [1973]. The secondary conveyor belt transports heat, moisture, and westerly momentum upward and poleward in relatively confined regions of flow within the storm [*Maue* 2010]. The conveyor belts associated with a warm seclusion have low air-sea gradients and moderate winds, anticipating lower heat fluxes in those regions.

Turbulent heat fluxes are important to the preconditioning, existence, and evolution of warm seclusions, but little is known regarding the immediate impacts these storms have on the air-sea fluxes caused by the strong winds associated with the bent-back frontal structure [*Maue,* 2010]. The area of large surface turbulent fluxes trails well behind the warm core, and is likely to play a larger role in regional energy budgets and climate, than in powering the cyclone. There are few direct observations of the component variables needed to compute the fluxes since ships and other observing platforms attempt to avoid such powerful storms. Satellite retrievals, particularly in the microwave region where clouds interfere less with observations [*Roberts et al*., 2010], can be used to obtain meaningful, representative data regarding the characteristics of warm seclusions. Comparatively, storms similar in size to warm seclusions have enormous turbulent fluxes and, depending on storm frequency, have a significant effect on regional energy budgets. The effects of warm seclusions on the turbulent heat fluxes have not been previously determined and are investigated as a preliminary demonstration of the importance of warm seclusions on the heat budget.

**Table 2-1:** From *Bourassa et al.* [2010a]. Accuracies and biases associated with the fluxes and component variables for particular applications. The values indexed by the table represent the significance associated with the particular variable relevant to the process under consideration.

| Variable | R/V or Direct Observation | NDBC Buoys | $CO_2$ Budget | Global Climate Change | Ice Sheet Evolution | Annual Ice Mass | Upper Ocean Heat Content | Open Ocean Upwelling | Dense Water Formation |
|---|---|---|---|---|---|---|---|---|---|
| Stress ($Nm^{-2}$) | Very small | NA | 0.01 | TBD | TBD | TBD | TBD | TBD | TBD |
| Sensible + Latent ($W\ m^{-2}$) | Very small | NA | - | < 0.25 | 0.5 | 2.5 | 5 | 5 | 5 |
| Vector Wind | 0.14 | | TBD | TBD | TBD | TBD | TBD | TBD | TBD |
| Wind Speed ($m\ s^{-2}$) | 0.2 | 1.0 | 1.0 | 0.01 | 0.02 | 0.1 | 0.2 | 0.2 | 0.2 |
| SST (K) | 0.1 | 1.0 | 2.5 | 0.005 | 0.01 | 0.05 | 0.1 | 0.1 | 0.1 |
| Air Temperature (K) | 0.2 | 1.0 | > 10 | 0.01 | 0.02 | 0.1 | 0.2 | 0.2 | 0.2 |
| Humidity ($g\ kg^{-1}$) | 0.3 | * | > 10 | 0.015 | 0.03 | 0.15 | 0.3 | 0.3 | 0.3 |

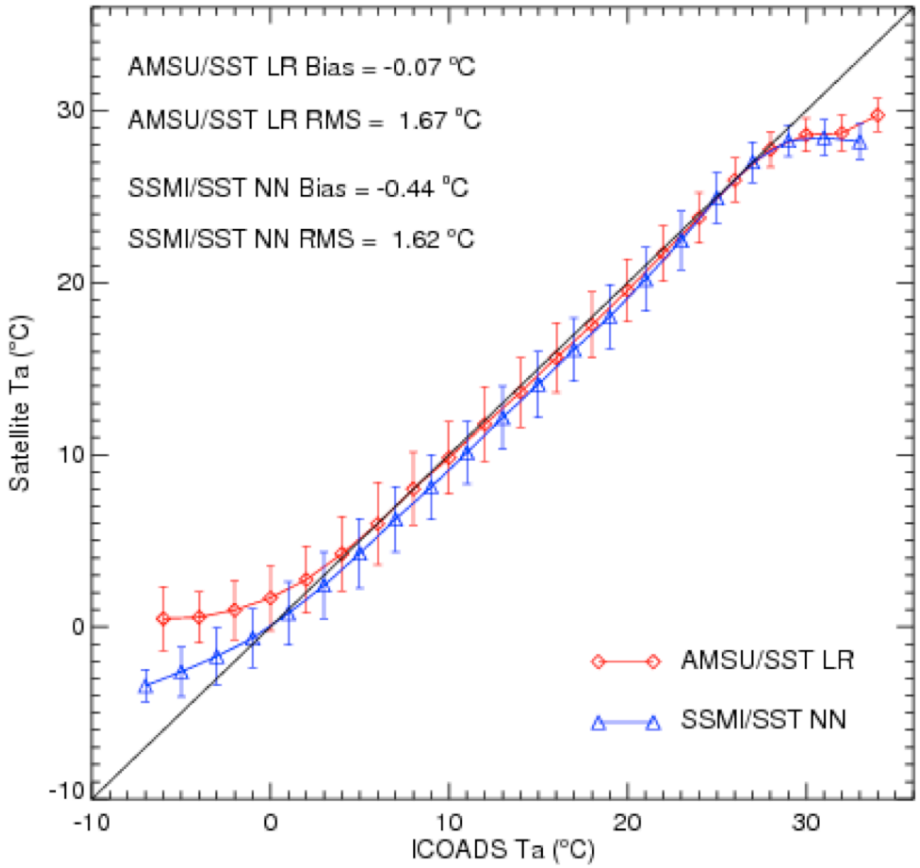


**Figure 2-1**: From *Bourassa et al.* [2010a] their Figure 4. Scatterplot of 10-m air temperature, height-adjusted ICOADS (International Comprehensive Ocean-Atmosphere Data Set) versus satellite-derived data. ICOADS serves as an in situ data set [*Smith et al.*, 2009] The red curve represents the multiple linear regression (LR) retrieval technique of *Jackson et al.* [2009]. The blue curve represents the neural network (NN) retrieval technique of *Roberts et al.* [2010]. Both perform well overall, but have biases near the extremes. The bias of the neural network retrieval technique is -0.44° C.

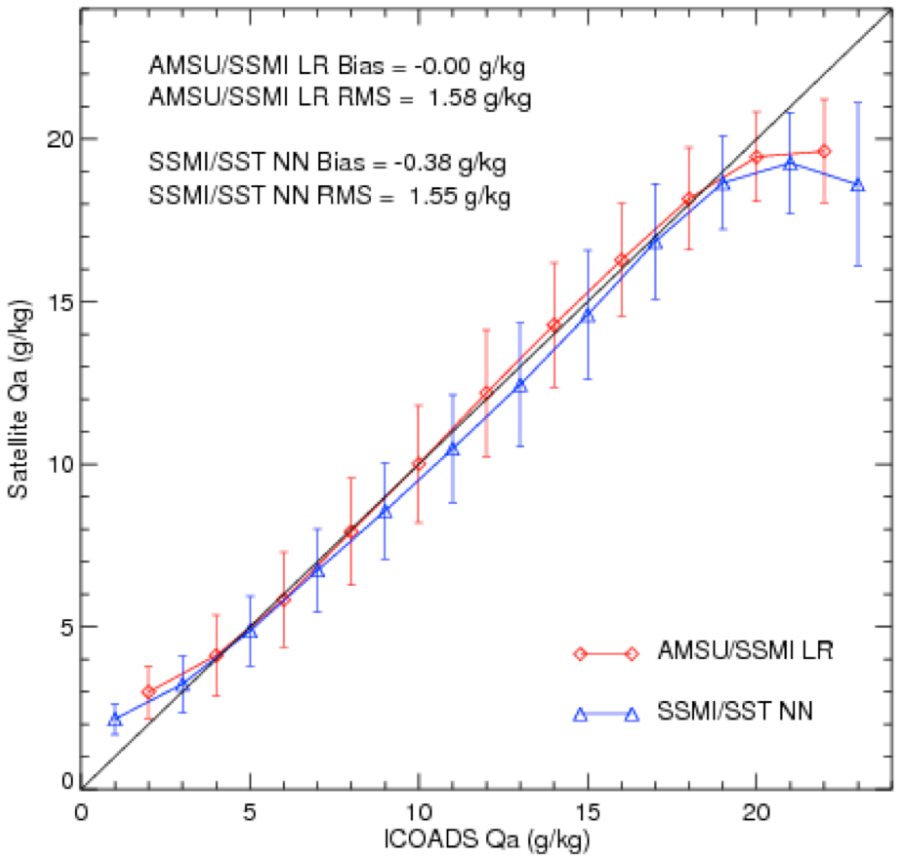


**Figure 2-2**: From *Bourassa et al.* [2010a] their Figure 4. Scatterplot of 10-m specific humidity, height-adjusted ICOADS (International Comprehensive Ocean-Atmosphere Data Set) versus satellite-derived data. ICOADS serves as an in situ data set [*Smith et al.*, 2009] The red curve represents the multiple linear regression (LR) retrieval technique of *Jackson et al.* [2009]. The blue curve represents the neural network (NN) retrieval technique of *Roberts et al.* [2010]. Both perform well overall, but have biases near the extremes. The bias of the neural network retrieval technique is -0.38 g/kg.

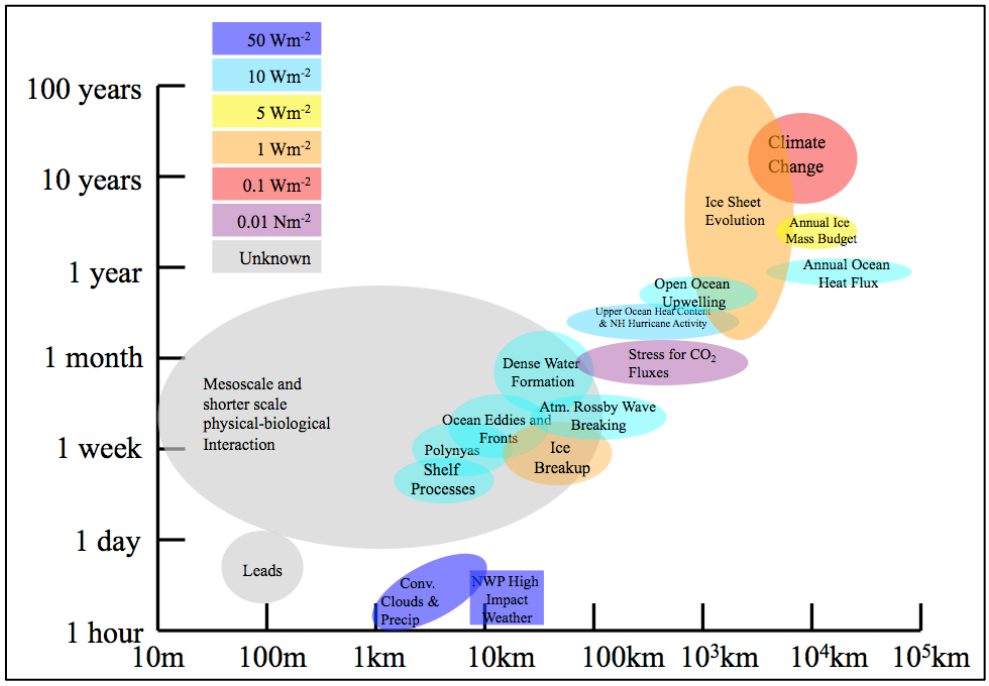


**Figure 2-3:** From *Bourassa et al.* [2010b]. Error values that are significant on varying time and spatial scales for relevant processes, ranging from 1 hour to 100 years and from 10 m to $10^5$ km. For most of these processes bias is the greatest concern.

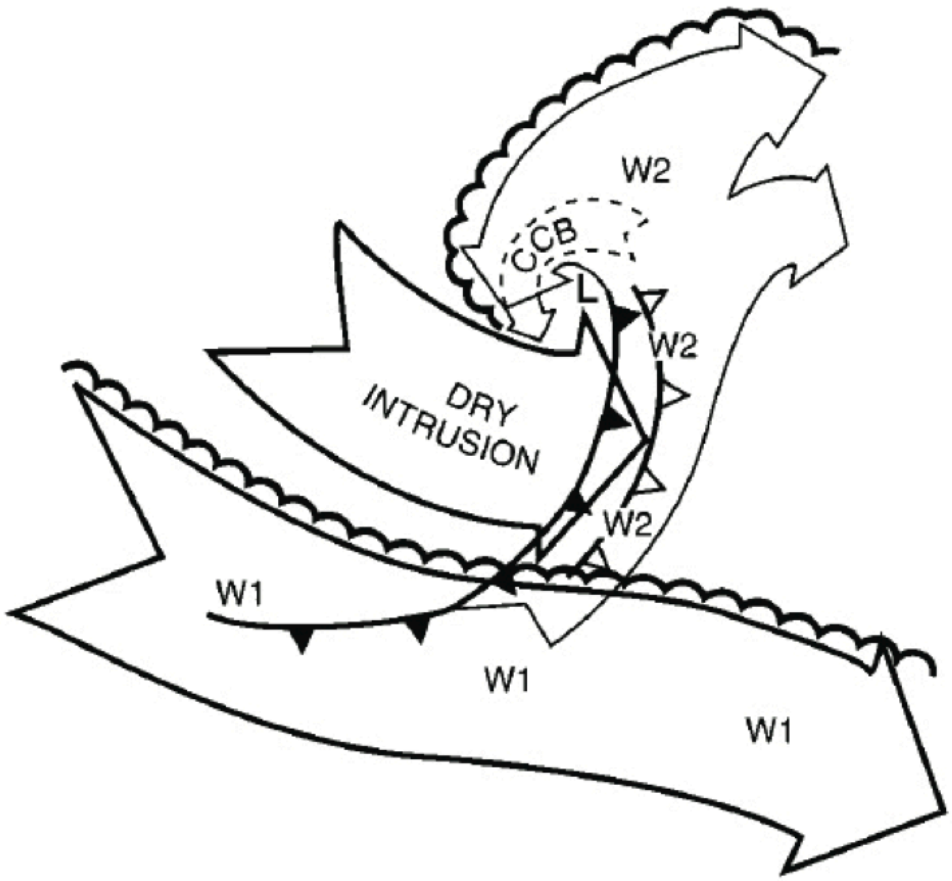


**Figure 2-4:** From Browning (1997) Figure 5. Caption: "Conceptual model showing system-relative airflow associated with the diffluent-flow type of cyclogenesis. The arrows labeled W1 and W2 are the primary and secondary warm conveyor belts. The dashed arrow labeled CCB is a cold conveyor belt. The dry intrusion is seen to overrun W2 over a broad region to produce an upper cold front at its leading edge. (After Young et al. 1994.)"

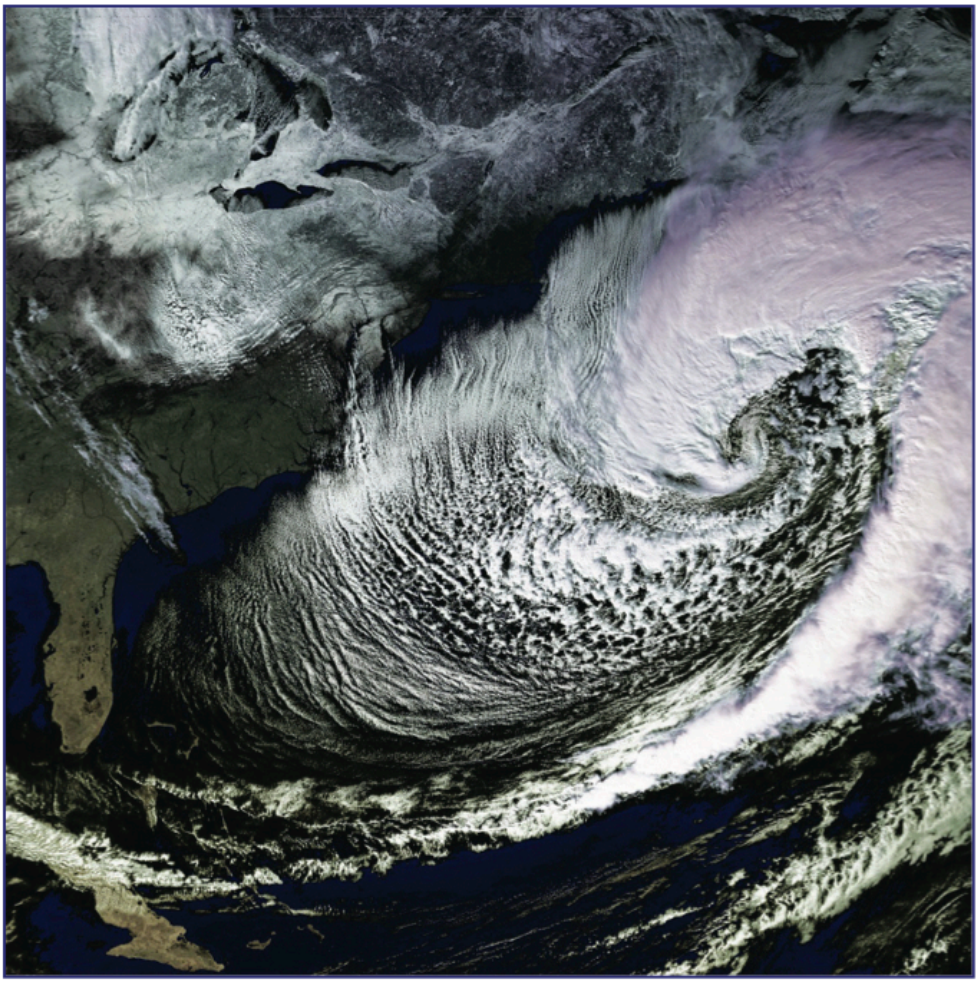

**Figure 2-5:** From *Maue* [2010] his Figure 2.1. Caption: "…Enhanced color visible AVHRR [Advance Very High Resolution Radiometer] NOAA 11 – HRPT January 04, 1989 17:51-18:03 UTC."

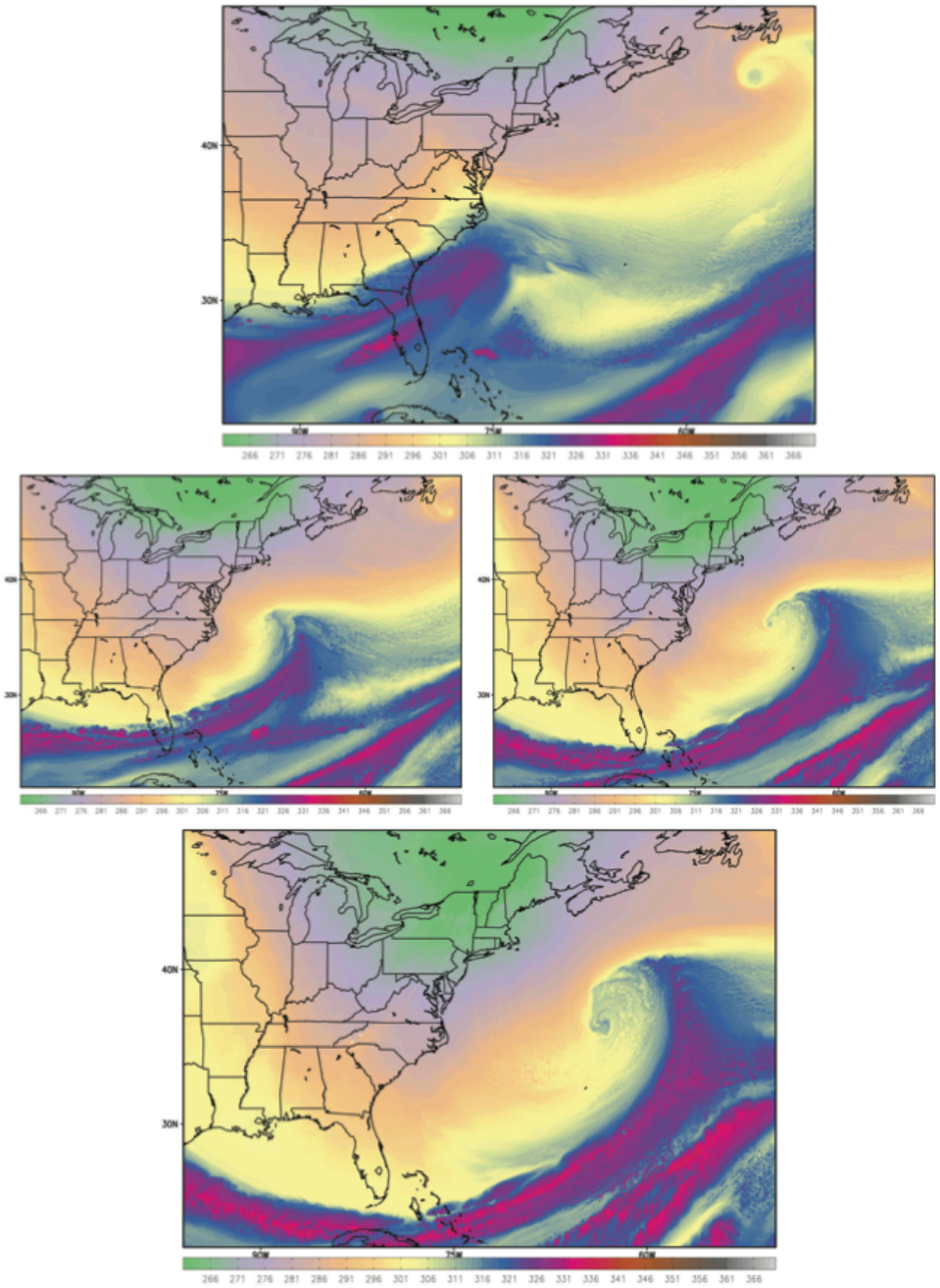

**Figure 2-6:** From *Maue* [2010] his Figure 2.11. Caption: "WRF [4km, 1750*x*1250*y*50L] hindcast simulation 850-hPa equivalent potential temperature [shaded $\theta_E$, Kelvins] for the ERICA IOP4 cyclone on 04 Jan 1989 at (a) 00Z (b) 08Z (c) 14Z and (d) 18Z."

# CHAPTER THREE

# METHODOLOGY

The turbulent heat fluxes associated with warm seclusions are not well understood. A small set of examples is used to illustrate likely errors in energy and moisture budgets associated with surface turbulent fluxes for warm seclusions as represented in several data sets. In conducting an intercomparison of the fluxes, a consistent flux computation algorithm is implemented to determine the fluxes in a physically consistent manner. Although a version of precomputed turbulent fluxes are provided with each data set, the fluxes are computed again from the component variables in each data set. This approach eliminates discrepancies that might be introduced into the fluxes by the use of varying flux algorithms and differing assumptions and computation methods (see Smith et al. [2010] for details on the algorithmic differences for the older products). Computing the fluxes in a physically consistent manner focuses the differences on the representation of these extreme weather systems in the data sets instead of on the flux computation method itself.

Neither satellite estimates nor numerically modeled data are considered to be "truth." Both types of data are representations of what is likely occurring. There are uncertainties and biases associated with both types. This study serves both as an intercomparison of estimates from interpolated satellite and reanalysis data and as a validation, since a comparison data set with known biases and error statistics is also being used to analyze these storms (section 3.2 and subsection 3.2.3).

## 3.1 Intercomparison methodology

The turbulent heat fluxes are computed using a modularized flux testbed (MFT) that allows various components of different flux models to be combined. An ideal flux model for large air/sea temperature differences and high wind speeds ranging from moderate to hurricane conditions does not exist. The Bourassa [2006] momentum flux parameterization (an updated version of the Bourassa-Vincent Wood (BVW) algorithm [*Bourassa et al.,* 1999]) has been shown to work well for high wind speeds (up to at least 24 $ms^{-1}$). However, observations and models indicate that different physical processes should be considered for hurricane force winds. There is no agreement in the scientific community on how these processes (e.g., sea spray

[*Andreas et al.*, 2008], rain [*Drennan et al.,* 2010], and sea state [*Powell et al.*, 2003; *Bourassa et al.*, 1999]) should be combined for heat fluxes in hurricane conditions. Most flux models greatly overestimate the fluxes for these conditions. The sea state adjustment in the Bourassa (2006) model addresses and minimizes these problems for subhurricane wind speeds. However, hurricane conditions are anticipated to produce an overestimated wind stress, which will slightly enlarge the sensible and latent heat fluxes. Recent models give highly contradictory results [*C. W. Fairall, Pers. Comm., 2006*; *Andreas*, 2004].

The original BVW model used the wall theory [*Bourassa et al.,* 1999] to estimate roughness length for potential temperature and humidity, which are used in the calculations of sensible and latent heat fluxes. The Bourassa [2006] model implemented the Clayson-Fairall-Curry (CFC) [1996] roughness length parameterization, and this parameterization is again selected in the MFT. Specifically, the CFC roughness length parameterization depends on the ratio of the mean wind speed at the height of the molecular interface to the friction velocity. The MFT includes a modification to this CFC parameterization [*Griffin,* 2009] to reduce a bias associated with the propagation of observational noise through several nonlinear operations. Additionally, the MFT allows for fluxes to be computed with either equivalent neutral winds (i.e., satellite-derived estimated wind; section 3.1.2) or traditional observed winds as input values.

The benefits of the MFT are three-fold. First, the MFT accurately handles a variety of input data with varying characteristics. These characteristics not only include different wind types, but also include varying reference heights of the input data. The MFT evaluates these data characteristics (e.g., different types of wind or humidity) and selects the appropriate method to handle the input fields in a physically consistent manner. Secondly, the MFT also incorporates multiple flux parameterizations, combining elements of several parameterizations to handle a wider range of atmospheric conditions (e.g. – strong versus calm wind speeds, etc.). The MFT can be used to select the appropriate flux model elements that are most suited to handle the environmental conditions for that point in time and space. Thirdly, the MFT options can be selected to ensure physically consistent flux calculations. The fluxes computed by the MFT can be selected to be physically consistent: for example, satellite winds can be ingested in a manner that accounts for the differences from traditional winds.

### 3.1.1 Flux computation algorithm

This project uses a look-up table version of the MFT. This version operates using input data in the form of fields or swaths of data on a global grid. Individual fields of pressure, air temperature, skin or sea surface temperature, moisture content of the air, moisture content at the surface, and wind speed are provided to the algorithm. The MFT then uses look-up tables to determine the appropriate heat, drag, and moisture transfer coefficients, on the basis of the input values at each specific grid point. The look-up tables are constructed from the computationally slower, iterative MFT. The bulk-aerodynamic formulae for LHF (1) and SHF (2) estimate the turbulent heat fluxes from the input variables and determined transfer coefficients. This algorithm generates a field of flux values on the same grid as the input data.

$$LHF = -\rho L_v q_* \left|\mathbf{u}_*\right| \approx \rho L_v C_e (q_{10} - q_{sfc}) \left|\mathbf{U}_{10}\right| \tag{1}$$

$$SHF = -\rho C_p \theta_* \left|\mathbf{u}_*\right| \approx \rho C_p C_h (\theta_{10} - \theta_{sfc}) \left|\mathbf{U}_{10}\right| \tag{2}$$

where $\rho$ is the air density, $L_v$ is the latent heat of vaporization, $q_*$ is the moisture scale factor, $\theta_*$ is the temperature scale factor, $\mathbf{u}_*$ is the friction velocity vector, $C_e$ is the moisture transfer coefficient, $C_p$ is the heat capacity, $C_h$ is the heat transfer coefficient, $q_{10}$ is the 10-m specific humidity, $q_{sfc}$ is the surface specific humidity, $T_{10}$ is the 10-m air temperature, $T_{sfc}$ is the surface temperature, and $\mathbf{U}_{10}$ is the 10-m wind vector.

### 3.1.2 Equivalent neutral wind

Satellites are able to measure winds by determining the ocean surface response to the stress caused by the wind. Wind stress produces surface capillary waves, which influence sea surface roughness [*Chelton and Wentz,* 2005; *Bourassa et al.,* 1999; *Liu and Xie,* 2006], and cause white capping at higher wind speeds. The microwave backscatter and emissions (for active and passive retrievals of winds) are calibrated to an equivalent neutral wind [*Kara et al.*, 2008; *Ross et al.*, 1985, *Liu et al.*, 1996], which is not the same as a traditional wind value. Equivalent neutral winds are derived using the nonneutral friction velocity and roughness length (which are analogous to what the satellite senses) and then are adjusted to a 10-m height using a neutral

boundary-layer stratification. A neutral value of the drag coefficient can be used to determine the kinematic stress. Therefore, the wind values in the satellite-based data are called equivalent neutral winds, whereas reanalysis winds are a value based on a variety of assimilated wind observations. Although satellite equivalent neutral wind retrievals are assimilated into the reanalysis data, the assimilation process treats them as traditional wind values (e.g., NCEP products) or adjusts then to real wind values (e.g., ECMWF products) with a global mean bias adjustment. Therefore, the reanalysis winds are considered traditional wind values.

The MFT operates using different versions of the look-up tables to handle the different wind inputs. One version of the tables is compatible with the satellite-derived data and includes the necessary modifications to compensate for equivalent neutral wind values. The other version of the tables is compatible with the reanalysis data and expects traditional wind values. Therefore, the MFT produces fluxes that are physically consistent, enabling an intercomparison of like quantities.

### 3.2 Data

This study uses two types of data to quantify the relationship between warm seclusions and the turbulent heat fluxes: satellite-derived data from the instrument-type known as Special Sensor Microwave/Imager (SSM/I) and numerically derived reanalysis data. Reanalysis data are generated by taking a fairly current numerical weather prediction configuration, freezing the model configuration, and assimilating multiple types of data to initialize and run the reanalysis. It is termed retrospective analysis, or reanalysis, since past observations are assimilated and input to the model, reanalyzing historic observations. The sources for the assimilated data include station data and observations, upper atmosphere information, ship and buoy observations, and selected quality-controlled, bias-corrected satellite data. Particularly relevant to this intercomparison are data originating from the ocean observing system, since this project's focus is on warm seclusions that occur over the oceans. Reanalyses utilize input data that came from the ships as well as moored and drifting buoy data; however, observations that provide an atmospheric profile (e.g., radiosondes) have a much greater weight than purely surface observations. Reanalyses often have difficulty modeling regions over the oceans, particularly the Southern Pacific, since data coverage is sparse away from radiosonde sites and outside shipping

routes and established buoy arrays However, improvements have been made through the assimilation of satellite data into the reanalysis over the South Pacific region.

### 3.2.1 Reanalysis data

Specific reanalysis data sets this study uses are CFSR [*Saha et al.,* 2010], ERA-Interim [*Simmons et al.,* 2007], MERRA [*Bosilovich et al.,* 2009], and NCEP-R2 [*Kanamitsu et al.,* 2002]. These data sets are chosen for the multiple perspectives of the fluxes provided by the differing model physics and parameterizations. These selected data sets include "state-of-the-art" reanalysis products, such as CFSR and MERRA, as well as older, more well studied reanalysis products, with known biases and parameterization issues, such as NCEP-R2. Table 3-1 summarizes the selected reanalysis products and their initial grid spacing in time and space. Table 3-2 presents a description of the units and variables that were used from each reanalysis data set as input values to the MFT.

To conduct the intercomparison, the data are regridded using a bilinear interpolation to a 0.25-degree by 0.25-degree uniformly spaced global grid with data spanning latitudinally from 89.875 degrees South to 89.875 degrees North and longitudinally from 0.125 degrees East to 359.875 degrees East. To place the data on the same temporal spacing, the six-hourly reanalysis data are bilinearly interpolated to a three-hourly resolution. For the one-hourly reanalysis data, center-point averaging focused on a three-hour averaging period is used. These requirements are chosen to match the SeaFlux satellite data set's spatial and temporal gridding (section 3.2.3).

### 3.2.2 Reanalysis specific and modifications

After regridding and interpolating, each data set undergoes other slight modifications to be compatible with the updated BVW flux computation algorithm. CFSR [*Saha et al.,* 2010], which is produced by the National Oceanic and Atmospheric Administration's National Centers for Environmental Prediction division (NOAA NCEP), is preprocessed to yield the surface specific humidity by assuming a 98 percent relative humidity. The Clausius-Clapeyron relation (3) is then used to compute the saturation vapor pressure ($e_s$), which is used to find the saturation mixing ratio. This ratio and the relative humidity are used to obtain the specific humidity at the surface before running the MFT algorithm. NCEP-R2 [*Kanamitsu et al.,* 2002], produced by the same division of NOAA as CFSR is, undergoes the same modification to obtain the desired quantities.

$$e_s = 6.11 \exp\left[\frac{(L_v)(T) - (273.15)(L_v)}{(273.15)(R_v)(T)}\right] \quad (3)$$

where $T$ is the temperature and $R_v$ is the gas constant for moist air.

The European Centre for Medium-Range Weather Forecasts' (ECMWF) ERA-Interim [*Simmons et al.,* 2007] is likewise preprocessed. The surface specific humidity is extracted assuming a 98 percent relative humidity at the surface and applying the Clausius-Clapeyron relationship (3). However, the specific humidity of the air is not provided as a part of ERA-Interim. Rather, the 2-m dew point temperature is given, which is converted using the Clausius-Clapeyron relation into a specific humidity valid for the same height as the dew point temperature provided in the data set.

MERRA [*Bosilovich et al.,* 2009] is produced by the National Aeronautics and Space Administration (NASA). The variables used to compute the fluxes for this intercomparison are from the one-hourly SLV (single-level variable) MERRA data subset. As with the CFSR and NCEP-R2 data sets, the surface specific humidity is not included directly in the reanalysis and is obtained by assuming a 98 percent relative humidity and implementing the Clausius-Clapeyron relation (equation 3). Additionally, the temperature and pressure units are adjusted to the inputs required by the flux computation algorithm.

### 3.2.3 Satellite data

The second type of data is satellite-derived data from the SeaFlux version 0.75 interpolated and uninterpolated data sets. These data sets are based on satellite observations from polar-orbiting satellite microwave imagers, specifically the instrument known as SSM/I. The SeaFlux data sets were created using the neural network methodology of *Roberts et al.* [2010] to extract the desired variables from the SSM/I data. The SeaFlux data sets are chosen on the basis of the successful results of the neural network regression technique [*Bourassa et al.,* 2010a], as seen in Figures 1-1 and 1-2.

Two SeaFlux version 0.75 data sets are used in this study. The first is the interpolated data subset, used for the intercomparison in the same manner as the reanalysis data [Section 4.1, 4.2, and 4.3]. The second data set is the uninterpolated, swath data, which is implemented for its ability to serve as a comparison data set since it has undergone neither smoothing nor

interpolation to distort the results. The fluxes derived from the SeaFlux uninterpolated data set are bias corrected [Section 3.3] and serve as comparison data.

Specific variables of the SeaFlux version 0.75 data sets have varying origins. The air temperature and specific humidity (both for a height of 10m) are derived from the SSM/I observed brightness temperatures using SSM/I observations and the neural network regression methodology [*Roberts et al.,* 2010]. The winds in the SeaFlux data sets are from Remote Sensing Systems' version 6 uninterpolated satellite microwave wind product [*Meissner and Wentz*, 2002; *Roberts et al.,* 2010]. These variables, for the interpolated data set, were provided on a 0.25-degree by 0.25-degree uniform global grid in 3-hourly data groupings. The uninterpolated data set's variables were provided in the form of swath data. Additionally, a uniform pressure field of 1013.25 hPa is used in the flux computation with the SeaFlux data set.

### 3.3 Bias correction

The biases and error characteristics for the SeaFlux version 0.75 uninterpolated component variable data have been determined by *Bourassa et al.* [2010a], through a comparison to height-adjusted ICOADS observations. These error characteristics are used to find the bias and random errors associated with the computed flux output from the MFT. The computed fluxes are found to be biased high. The biases are subsequently removed from the turbulent heat fluxes produced from the uninterpolated comparison data. Typical biases associated with the LHF vary from less than 10 $Wm^{-2}$ away from the storm to roughly 50 $Wm^{-2}$ near the core of a warm seclusion [Figures 3-1, 3-2, and 3-3]. For the SHF, the biases are also less than 10 $Wm^{-2}$ away from the storm and roughly 30 $Wm^{-2}$ near the storm's core [Figures 3-1, 3-2, and 3-3]. Storm-specific details and the bias-corrected fluxes for each of these warm seclusion cases can be found in Sections 4.1, 4.2, and 4.3.

### 3.4 Warm seclusion identification

Three specific warm seclusion events were identified to conduct the intercomparison of the selected data sets. These warm seclusions were chosen on the basis of a selection and storm-sorting algorithm developed by Maue [2010]. The algorithm identifies these storms using specific pressure and formation characteristics associated with warm seclusions. Specifically, a storm must undergo explosive deepening, defined as ≥24 hPa per 24-hour period times the cosine of the latitude [*Saunders and Gyakum*, 1980; *Maue*, 2010]. Once a storm is identified,

Maue's algorithm forms a storm track through a location and duration analysis using pressure data from the MERRA reanalysis [R. N. Maue Pers. Comm, 2010]. This algorithm identified over 460 warm seclusion events globally, for the period from August 2003 to March 2007.

From these identified storm events, further criteria are used to select specific cases for this study. The specific cases are chosen to be geographically diverse, occurring in different ocean basins. Geographic variety allows the fluxes associated with warm seclusions to be evaluated in multiple regions. Additionally, storm events that are relatively isolated from other convective events and warm seclusion activity are desired. This condition focuses the analysis on the fluxes resulting from the chosen warm seclusion while minimizing possible fluxes from other sources, which might skew the results. Data availability also influences the case selection. Data from all six data sets for the time, location, and duration of each storm is required and reduces the number of usable cases. Maue's algorithm identified over 460 storm events during a 3 year period; however, the filtering process reduced the number of cases under consideration to three, a North Pacific case, a South Pacific case, and a North Atlantic case.

**Table 3-1**: Temporal and spatial characteristics of the two types of data involved in this study: reanalysis and satellite. These are the original data specifications prior to spatial regridding and temporal interpolation (or averaging as the data set necessitates). From *Saha et al.* [2010], *Simmons et al.* [2007], *Bosilovich et al.* [2009], *Kanamitsu et al.* [2002], and *Roberts et al.* [2010].

| | Reanalysis Data | | | | Satellite Data |
|---|---|---|---|---|---|
| | CFSR | ERA-Interim | MERRA | NCEP-R2 | SeaFlux |
| Temporal | 6 hourly | 3 hourly | 1 hourly | 6 hourly | 3 hourly |
| Latitudinal | T382 Gaussian | 0.6666° | 0.5° | T62 Gaussian | 0.25° |
| Longitudinal | T382 Gaussian | 0.6666° | 0.6666° | T62 Gaussian | 0.25° |

**Table 3-2**: Variable availability per data set for both reanalysis and satellite data. Units are included for comparison. A blank entry indicates that variable is not available for that data set. These are the units the data set provides, before conversion to the desired format for the updated BVW flux computation algorithm. From *Saha et al.* [2010], *Simmons et al.* [2007], *Bosilovich et al.* [2009], *Kanamitsu et al.* [2002], and *Roberts et al.* [2010].

| | Reanalysis Data | | | | Satellite Data |
|---|---|---|---|---|---|
| | CFSR | ERA-Interim | MERRA | NCEP-R2 | SeaFlux |
| Dew Point (2-meters) | | Kelvin | | | |
| Specific Humidity (2-meters) | kg/kg | | | kg/kg | |
| Specific Humidity (10-meters) | | | kg/kg | | g/kg |
| Surface Pressure | Pascals | Pascals | Pascals | Pascals | Pascals |
| Sea Surface Temperature | | Kelvin | | | Celsius |
| Skin Temperature | Kelvin | | Kelvin | Kelvin | |
| Air Temperature (2-meters) | Kelvin | Kelvin | | Kelvin | |
| Air Temperature (10-meters) | | | Kelvin | | Celsius |
| Wind Speed | | | | | m/s |
| U-component (10-meters) | m/s | m/s | m/s | m/s | |
| V-component (10-meters) | m/s | m/s | m/s | m/s | |

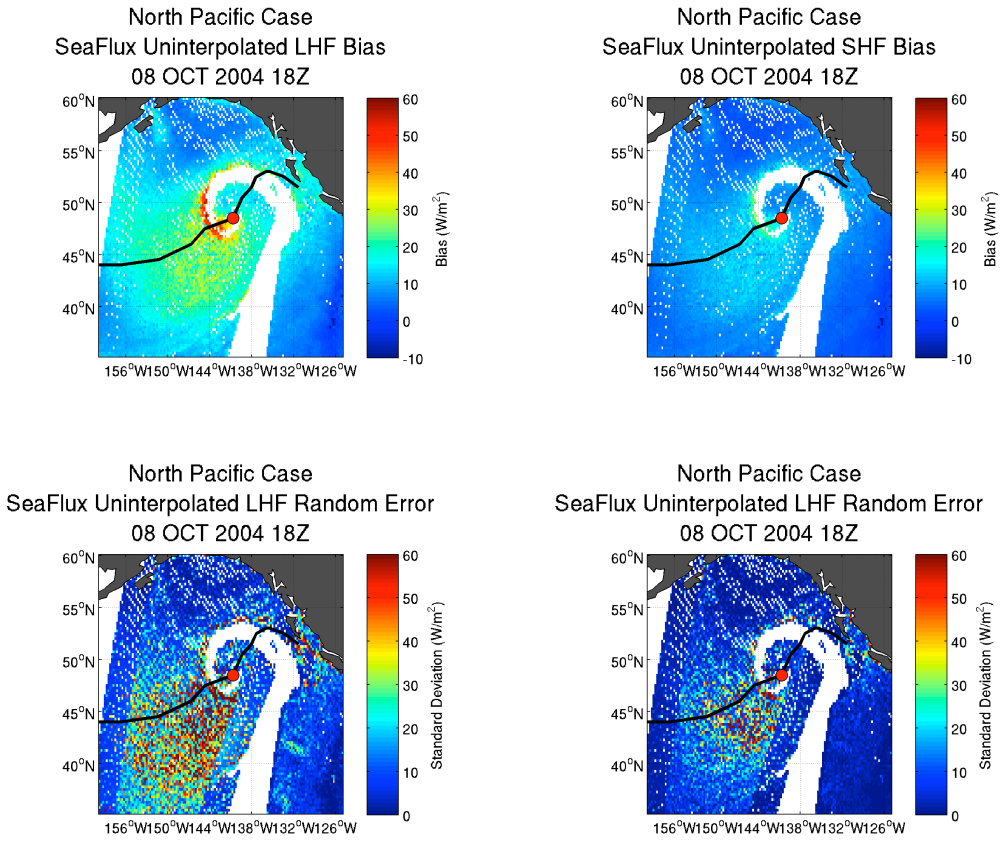


**Figure 3-1**: The bias (top row) and random error (bottom row) for LHF (left column) and SHF (right column) associated with the SeaFlux uninterpolated swath comparison data set, valid for 08 October 2004 18Z. The black line indicates the track of the warm seclusion from Maue [2010]'s algorithm. The red dot indicates the center of the warm seclusion.

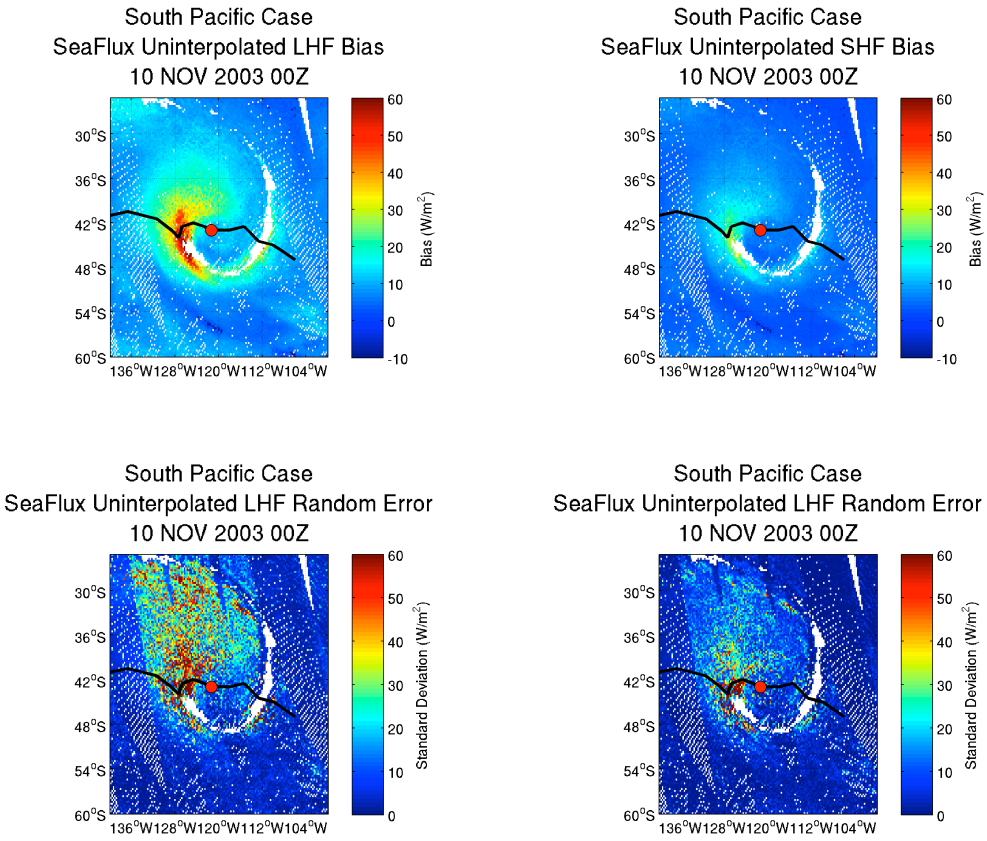


**Figure 3-2**: The bias (top row) and random error (bottom row) for LHF (left column) and SHF (right column) associated with the SeaFlux uninterpolated swath comparison data set, valid for 10 November 2003 00Z. The black line indicates the track of the warm seclusion from Maue [2010]'s algorithm. The red dot indicates the center of the warm seclusion.

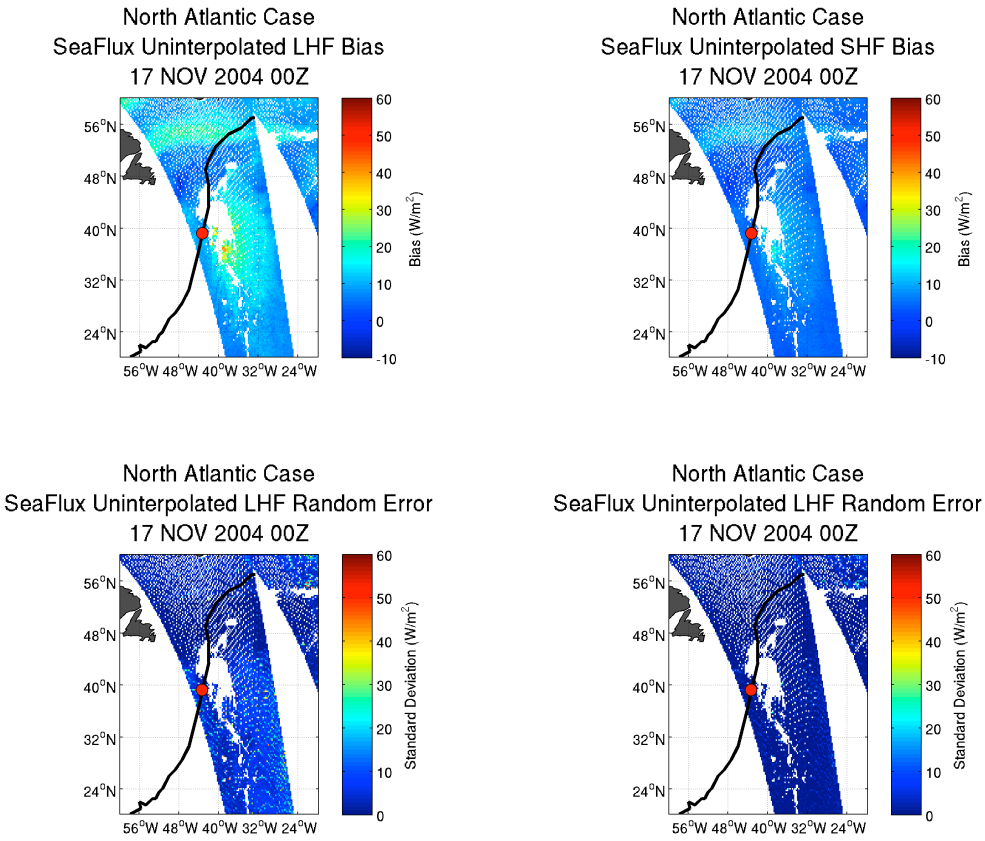


**Figure 3-3**: The bias (top row) and random error (bottom row) for LHF (left column) and SHF (right column) associated with the SeaFlux uninterpolated swath comparison data set, valid for 17 November 2004 00Z. The black line indicates the track of the warm seclusion from Maue [2010]'s algorithm. The red dot indicates the center of the warm seclusion.

# CHAPTER FOUR

# RESULTS AND DISCUSSION

Three warm seclusions, identified by the methodology of Maue [2010], are analyzed herein. Specifically, they are a North Pacific case, a South Pacific case, and a North Atlantic case. The North Pacific warm seclusion case began in the West Pacific on 05 October 2004 and traveled east toward the southern coast of Alaska on a fairly east-west oriented path (Figure 4-1) until it dissipated on 09 October 2004, lasting for a period of nearly five days. The South Pacific case began off the coast of New Zealand, and propagated to the east, toward the southern tip of South America with a mostly east-west oriented track with a slight tilt to the south (Figure 4-1). This warm seclusion event began on 05 November 2003 and lasted until 12 November 2003. The third warm seclusion under consideration occurred between 13 November 2004 and 20 November 2004. This case was first classified as a warm seclusion just outside the Caribbean Sea (Figure 4-1) and dissipated south of Iceland, off the coast of Greenland. It traveled primarily north-south with a slight eastward tilt.

Each case undergoes two types of analysis: instantaneous spatial examination and a time-integrated total flux analysis. The instantaneous spatial plots are used to evaluate the regions of peak fluxes and determine an instantaneous value for the LHF and SHF for each storm. These plots are also used to compare the spatial variations that exist among the data sets. The instantaneous spatial plots are analyzed at three different instances in the warm seclusion's life cycle to visualize the evolution of the storm and the associated turbulent heat fluxes. The time-integrated analysis is used to evaluate the contribution of these storms to the regional energy budget by computing the monthly distributions of the total fluxes for a storm-centric region and for the ocean basin. A comparison of these flux distributions indicates what fraction of the monthly heat fluxes is generated by the storm.

## 4.1 North Pacific warm seclusion case

The instantaneous LHF values for the North Pacific warm seclusion case are depicted in Figures 4-2, 4-3, and 4-4, each corresponding to a different time in the life of the storm. The earliest snapshot of the fluxes (Figure 4-2) depicts the computed fluxes from all six data sets at 06 October 2004 00Z. At this time, the warm seclusion is in its early stage of development, when

the frontal structure and bent-back shape are yet to evolve. At the center of the storm, only low fluxes are observed (less than 100 $Wm^{-2}$), associated with the warm front and low air-sea differences that dominate the storm at this point in its lifetime. Ahead of the storm, the leading cold front can be identified as the region of higher fluxes. There is some variation between the data sets at this time. Specifically, the SeaFlux interpolated data set is not resolving the leading cold front well, especially towards the equator. MERRA has comparatively low values across the field relative to the SeaFlux uninterpolated comparison data. Conversely, ERA-Interim and CFSR are producing rather broad regions of high LHF values over 300 $Wm^{-2}$, a feature not seen in the satellite data. (Recall, the fluxes associated with the reanalyses are modeled fluxes from the MFT, derived using the reanalyses' winds, temperatures, humidities, etc. and not the fluxes provided in the model data sets.)

The next snapshot of the LHF, on 07 October 2004 00Z, the storm is further developed in terms of the frontal structure and the bent-back shape is beginning to become identifiable in LHF fields (Figure 4-3). CFSR, ERA-Interim, and MERRA clearly resolve two maxima (200-300 $Wm^{-2}$) in the fluxes, one located just ahead of the storm center corresponding to the fluxes produced by the leading cold front. The maximum in the fluxes to the rear of the system is located behind the trailing cold front, which contains relatively high air-sea specific humidity differences. The region of low flux values between the maxima corresponds to the secondary warm conveyor belt, containing low air-sea differences. The fluxes in area of the trailing maxima are amplified by the dry intrusion from the rear associated with high wind speeds. As time progresses, this region behind the trailing cold front develops into the primary region of high fluxes associated with the warm seclusion. However, at this time, the frontal structure has not yet fully developed, with the warm occlusion still growing and the fronts wrapping tighter around the core. At this intermediate growth stage in the warm seclusion's lifecycle, the SeaFlux interpolated data set is not resolving the frontal boundaries well. This is likely due to the interpolation scheme used in the production of the original data set to fill the missing data from the gaps in the uninterpolated SeaFlux swath-based data. MERRA appears to be underestimating the LHF values associated with the warm seclusion by roughly 100 $Wm^{-2}$. NCEP-R2 is not resolving the frontal structure well and is producing a single region of high fluxes occupying the entire area to the rear and south of the storm. This is likely due to the low native resolution of the data set, inhibiting the region of low fluxes associated with the warm front from being resolved.

It is hard to verify the specific frontal structure in the satellite data due to a gap in between the swaths in this data set for this specific time.

The third LHF snapshot is at 08 October 2004 18Z (Figure 4-4) and depicts the mature stage of the warm seclusion's life cycle. In these panels, the fluxes associated with the trailing cold front have developed further reaching magnitudes in excess of 350-400 $Wm^{-2}$ (depending on the data set under consideration). These flux values are driven by the dry intrusion from the rear producing strong winds and the high air-sea differences associated with the cold air over the relatively warm water. It is noteworthy that these fluxes are roughly an order of magnitude greater than the background fluxes for this region, which are around 40 $Wm^{-2}$.

Similar comparative behavior is noticed in the data sets as seen in the earlier snapshots. MERRA performs well spatially in resolving the location of the maximum fluxes and the spatial extent but is underestimating the flux magnitude relative to the comparison data. NCEP-R2 has the peak fluxes occurring rather close to the core and further to the north than where these fluxes occur in the other data sets. ERA-Interim appears to be resolving the warm front and bent-back shape associated with the warm seclusion well, and all the reanalysis products seem to be accurately resolving the occluded warm air in the northeast quadrant near the core. The SeaFlux interpolated data set appears to not capture the frontal structure well and is noisy with patchy regions of high fluxes mingled throughout the region behind the trailing cold front. This indicates that the gradients associated with this warm seclusion are not well captured in the interpolated SeaFlux data set. This trend may possibly be arising due to the interpolation mechanism used to fill the gaps between the swaths and the missing data from rain contamination of the initial microwave imager data. Also note that the LHF from the SeaFlux uninterpolated data set has undergone bias correction. Fields of bias and random error for 08 October 18Z are shown in Figure 3-1. However, bias correction was conducted on all fluxes produced from this data set for all times [Section 3.3]. As expected, regions of higher flux have higher bias associated with them.

To understand why high values of LHF are resulting from this storm, the air-sea specific humidity difference (Figure 4-5) and wind speed (Figure 4-6) are analyzed for 08 October 2004 18Z. High specific humidity differences trail the cold fronts of the system due to the relatively cool, dry air contrasting with the warm, moist sea surface. The region of high specific humidity behind the trailing cold front is divided in two by the primary warm conveyor belt; this feature is

seen in all the data sets except for the comparison data, where the conveyor belt lies outside the plotted spatial domain.

The peak air-sea specific humidity differences do not match up spatially with the peak LHF values. Recall that the LHF also depends on wind speed (Figure 4-6). A clear cyclonic wind pattern is seen in all the data sets with peak wind speeds located near the core. This is especially true for the NCEP products: CFSR and NCEP-R2, which have higher wind speed values compared to the wind speed of the other data sets. CFSR and NCEP-R2's region of high wind speeds encircle the core almost completely. SeaFlux interpolated, MERRA, and ERA-Interim have high wind speeds concentrated more strongly in the southwest quadrant of the system, located in the region behind the trailing cold front where the dry intrusion is found. SeaFlux interpolated, MERRA, and ERA-Interim agree fairly closely with the comparison data. The spatial location of the air-sea differences and the high wind speeds, therefore, explain the region of high fluxes associated with the trailing cold front and dry intrusion to the rear of the warm seclusion.

The instantaneous SHF values for the North Pacific warm seclusion are depicted at three snapshots in time in Figures 4-7, 4-8, and 4-9. The earliest time, 06 October 2004 00Z, indicates low SHF values (less than 30 $Wm^{-2}$) near the core of the system, characteristic of the warm front dominating the storm. These flux values are close to the background SHF values for this ocean basin. A faint region of higher fluxes is seen ahead of the storm (Figure 4-7), where the leading cold front is located.

The warm front is located between the leading and the trailing cold fronts at 07 October 2004 00Z. Two SHF maxima appear (Figure 4-8) due to the air-sea temperature differences associated with the cold fronts combined with high wind speeds associated with this storm. Of the reanalysis data sets, CFSR and ERA-Interim resolve the two regions the most distinctly. However, the fluxes associated with the leading cold front are weaker relative to the SHF values associated with the trailing cold front, due to the winds in this quadrant of the storm being comparatively weaker than the winds associated with the trailing cold front and the dry intrusion. At this time, the frontal structure is still developing and wrapping around the system, and the SHF values associated with the warm seclusion have not yet reached their peak value. The reanalysis data sets also show contrasting features among themselves. CFSR and MERRA both underestimate the SHF relative to the comparison data, and NCEP-R2 has a rather confined

region of high fluxes focused at the storm's center. Overall, ERA-Interim performs well, capturing the region of high SHF magnitude and its spatial extent to the north.

At the mature stage of the warm seclusion, (08 October 2004 18Z; Figure 4-9), peak instantaneous SHF values are seen in excess of 100-150 $Wm^{-2}$, depending on the data set under consideration. The highest SHF values are located in the southwest quadrant of the storm, behind the trailing cold front where the dry intrusion from the rear is located. ERA-Interim and SeaFlux Interpolated appear to capture both the spatial extent and magnitude well, relative to the comparison data. MERRA underestimates the fluxes by roughly 100 $Wm^{-2}$, however, resolves the spatial extent of the storm's fluxes well. CFSR and NCEP-R2 are indicating regions of high fluxes but are not locating them well. NCEP-R2 places the high fluxes close to the core, a pattern not completely accurate relative to the comparison SeaFlux data. CFSR captures the magnitude of the SHF, but is spatially restricted, not occupying this region fully, compared to the satellite comparison data.

The regions of high SHF values are explained in the context of the wind speed (Figure 4-6) and air-sea temperature difference (Figure 4-10). High wind speeds are located around the core of the warm seclusion and are found behind the trailing cold front with the dry intrusion (Figure 4-6), as noted previously in the discussion of the LHF. The air-sea temperature differences are highest behind the bent-back region and the trailing cold front. CFSR, MERRA, and NCEP-R2 all seem to underestimate the magnitude and spatial extent of this region with respect to the air-sea temperature differences (Figure 4-10). Both SeaFlux data sets and ERA-Interim show agreement with the magnitude and the spatial extent, including the protrusion of high air-sea temperature differences north of the storm track. However, the SeaFlux interpolated data does not capture the frontal structure or the bent-back shape well.

The evolution in time of the turbulent heat fluxes as the warm seclusion develops its frontal structure, bent-back shape, and occluded warm air is characteristic behavior for warm seclusions examined in this study. The other two storm cases are analyzed identically with the three snapshots at similar stages in the warm seclusions' lifecycles. The fluxes behave in a very similar manner to this North Pacific case. Therefore, the images corresponding to the earlier times are omitted for the remaining two cases.

To determine the importance of the turbulent heat fluxes associated with a warm seclusion relative to the monthly averaged total heat flux of the ocean basin, box and whisker

analyses are conducted. Three time-integrated flux fields are computed for both LHF and SHF. The three integrations are (1) a storm-centric moving box integration (box size: 22° x 18°), (2) a total monthly ocean basin integration, and (3) a total monthly ocean basin integration without the storm event. The results of these analyses are presented in Figures 4-11 and 4-12 for LHF and SHF, respectively. The comparison data set is not included in this part of the analysis because errors would be introduced by the irregularity of the spatial and temporal sampling. From these analyses, the ratios of the 50th percentiles of the storm-only to the total monthly ocean basin time-integrated fluxes are listed in Table 4-1. The values of this diagnostic associated with this one warm seclusion range between 13-17% of the total monthly ocean basin LHF. This same diagnostic for the SHF is 16-21% of the total monthly ocean basin value (recall that this storm lasted only 5 of the 31 days in the month, covering roughly 30% of the ocean basin domain during those days). Therefore, the warm seclusion makes a disproportionally large contribution to the total monthly surface turbulent fluxes. It is also noteworthy that, compared to the reanalyses, the interpolated SeaFlux data set is on the high end of the ratio range for the LHF and on the low end for the SHF. The large fluxes occur during a small portion of the warm seclusion's lifecycle, during the mature stage, yet account for a relatively large portion of the monthly flux total.

## 4.2 South Pacific warm seclusion case

The South Pacific warm seclusion case differs from the North Pacific in that the storm's spatial layout is mirrored about the equator. The warm seclusion still propagates from west to east. However, the bent-back frontal structure arcs from the core of the storm north toward the equator and back to the west. This is especially noticeable in the latter stages of the warm seclusions lifecycle, when the region of high turbulent heat fluxes behind the trailing cold front is located to the northwest of the storm's core (Figure 4-13), compared to its location to the southwest of the core in the North Pacific case. In both cases, the area of high fluxes is behind the trailing cold front and towards the equator.

An instantaneous spatial plot of the LHF values is depicted in Figure 4-13 for 10 November 2003 00Z. This time corresponds to the third snapshot of the warm seclusion's lifecycle. As mentioned, three instantaneous spatial analyses of the storm are conducted, but only the plot from the mature stage of the storm is included. The LHF values at the earliest time, 06

November 2003 00Z, indicate that the storm is dominated by the warm front with low fluxes dominating the storm (around 50 $Wm^{-2}$), similar to the background LHF of the ocean basin. The trailing cold front is clearly identifiable behind the warm front and is driving the frontal bending and storm development.

At the next snapshot, 08 November 2003 00Z, the characteristic shape of the warm seclusion has formed. The warm front is associated with the region of low fluxes due to low air-sea differences, and the trailing cold front is seen behind the warm front and is associated with fluxes ranging from 250-300 $Wm^{-2}$. However, at this time in the storm, the frontal, bent-back structure is still developing and further wrapping into the storm. During this process, the dry intrusion strengthens, and the fluxes grow.

By 10 November 2003 00Z (Figure 4-13), the warm air is occluded to the southeast of the core, the warm front appears as a bent back region of low fluxes, and the trailing cold front contains LHF values in excess of 300-400 $Wm^{-2}$, depending on the data set under consideration. MERRA, for example, is underestimating the fluxes by approximately 100 $Wm^{-2}$, relative to the comparison data, and CFSR appears to be overestimating the LHF and placing the peak flux region too far to the north. ERA-Interim is resolving the spatial distribution well, but also seems to overestimating the LHF, and NCEP-R2 shows two regions of high LHF, which is not entirely justified by the comparison data but may be logical in the context of where the primary warm conveyor belt is located within the warm seclusion. All of the reanalysis data sets appear to resolve the frontal structure fairly well, whereas the SeaFlux interpolated data set is rather noisy, and does not resolve the warm occlusion to the southeast of the storm or the warm front well. However, this data set captures the magnitude and spatial extent of the fluxes behind the trailing cold front, relative to the comparison SeaFlux uninterpolated data set (which has undergone bias reduction using the bias data depicted in Figure 3-2 [Section 3.3]).

The spatial patterns of the LHF are driven primarily by air-sea specific humidity differences (Figure 4-14) and wind speed (Figure 4-15). High air-sea specific humidity differences are seen behind the trailing cold front and towards the equator. This is due to the cold air having greater differences in temperature and humidity compared to the surface values. The specific humidity differences are higher near the equator where the SSTs are warmer, leading to higher surface specific humidity according to the Clausius-Clapeyron relation. This is a trend seen in all the data sets, with ERA-Interim, CFSR, and SeaFlux interpolated matching the

comparison data fairly closely. Additionally, all the reanalyses seem to capture the warm front and it's structure well. However, MERRA resolves this feature the best, relative to the SeaFlux uninterpolated comparison data.

The wind speeds associated with the core and trailing cold front of the South Pacific warm seclusion exceed 15 $ms^{-1}$ for 10 November 2003 00Z (Figure 4-15). ERA-Interim and MERRA capture the spiral pattern of the winds about the core and resolve the magnitude of the winds associated with the dry intrusion from the rear well. CFSR and NCEP-R2 appear to indicate high wind speeds occupying a much broader region spatially relative to the comparison data, and the SeaFlux interpolated data set does not resolve the spiral pattern well. However, the extent of high wind speeds behind the trailing cold front, due to the dry intrusion, explains why the high flux values are seen in that region.

The SHF behaves in a similar manner to the LHF in regards to evolution of the storm in time. At the earliest snapshot, low SHF values are found, comparable to the background fluxes of the region. At this time, the warm front dominates the system and the air-sea differences are small, typical of the conditions away from the WCS. Larger SHF values develop behind the trailing cold front, and by 10 November 2003 00Z (Figure 4-16), a region of high SHF values is clearly seen behind the trailing cold front. Both SeaFlux data sets indicate peak fluxes values over 150 $Wm^{-2}$. The reanalysis data sets underestimate the SHF, particularly MERRA and NCEP-R2. CFSR and ERA-Interim both have peak values around 100 $Wm^{-2}$ in the region just behind the trailing cold front, where relatively high air-sea temperature differences (Figure 4-17) are observed and high wind speeds are located associated with the dry intrusion. In general, the reanalyses properly resolve the spatial location and structure of the region of high SHF values, with MERRA and ERA-Interim capturing the bent-back warm front well.

The discrepancy between the satellite-based data sets and the reanalyses in reference to the SHF magnitude appears to be stemming from the air-sea temperature differences (Figure 4-17). Both SeaFlux interpolated and uninterpolated data sets indicate differences greater than 4.5 K, while the reanalyses indicate values less than 4 K for the region behind the trailing cold front. The reanalyses also have more spatially confined high air-sea temperature differences with well-defined regions of low temperature differences associated with the warm front. NCEP-R2 appears to be the most different from the comparison data with the lowest magnitudes of the air-sea temperature difference.

The three box and whisker analyses for both LHF and SHF are also computed for the South Pacific case to evaluate the contribution of the warm seclusion's fluxes to the monthly ocean basin total fluxes. The resultant plots are included in Figure 4-18 for the LHF and Figure 4-19 for the SHF. CFSR has the greatest spread in all three of the LHF analyses and has the highest mean of the five data sets under consideration. Comparatively, MERRA has the lowest values and a smaller spread. It is also evident that by including the warm seclusion, the data sets' mean LHF values are increased. For the analyses of the SHF, the reanalyses data sets undergo a slight decrease in their respective means by the inclusion of the warm seclusion. The SeaFlux data set, however, by including the warm seclusion, experiences a substantial increase in the mean and upper percentiles. Table 4-2 summarizes the ratio of the 50th percentiles of the storm-only values to the monthly ocean basin total values for LHF and SHF, respectively. For the LHF, the mean of the storm-only analysis is 29-32% of the monthly ocean basin total integrated LHF (recall that the warm seclusion lasted for 7 of the 30 days in the month, and occupied roughly 25% of the ocean basin). The corresponding diagnostic for the SHF has a significant variation between the data sets (Table 4-2).

## 4.3 North Atlantic warm seclusion case

Occurring in the Northern Hemisphere and having the same spatial structure as the North Pacific warm seclusion, the North Atlantic warm seclusion case is complicated by the western boundary current (i.e. the Gulf Stream). The western boundary current is an ocean current that travels along the western boundary of an ocean basin and transports warm water from the southern latitudes to the cooler waters further north. In general, western boundary currents are often associated with regions of high fluxes since the air-sea differences are greater for those regions. The fluxes from the Gulf Stream can be seen clearly during the early stages in the warm seclusion's life (16 November 2004 00Z), when the storm is dominated by the warm front and the fluxes from the storm itself are low. At this time, large LHF values occur off the East Coast of the United States where the western boundary current is located. LHF values reach approximately 400 $Wm^{-2}$. CFSR overestimates the LHF in this region, and MERRA underestimates it, relative to the comparison data. Both ERA-Interim and NCEP-R2 appear to perform rather well in capturing the flux magnitude and spatial extent of the Gulf Stream's

contribution to the LHF. As mentioned the warm seclusion itself is dominated by the warm front with weak LHF values and the frontal structure just beginning to develop.

By 17 November 2004 00Z (Figure 4-20), the instantaneous LHF values associated with the warm seclusion become noticeably stronger than the surrounding fluxes, as the fluxes in the region behind the trailing cold front reach above 500 $Wm^{-2}$. The North-South orientation of storm track yields a frontal structure of the storm that has a greater spatial distribution compared to the warm seclusions in the other two cases. The warm front can be identified bending back from the core towards the equator and towards the Caribbean Sea, and the warm occlusion is seen to the north of the system's core, in the region of low LHF values off Newfoundland. These features are clearly identifiable in CFSR, ERA-Interim, and MERRA. The SeaFlux interpolated data set does not resolve the frontal structure and component gradients well, and the SeaFlux uninterpolated comparison data suffers from sparse data due to rain contamination of the satellite data and gaps in between the satellite's swaths. Certain trends associated with warm seclusions are still apparent in the data sets. For example, the high fluxes are observed behind the trailing cold front. For this warm seclusion case, these high LHF values are likely due to a three contributing factors, including the strong winds associated with the dry intrusion from the rear, the cool, dry air behind the trailing cold front, and the warm water transport to the north by the western boundary current.

The contribution of the western boundary current to the fluxes can bee seen in the air-sea specific humidity differences (Figure 4-21). Since the surface specific humidity is dependent on SST, the Gulf Stream stands out as a region of high specific humidity difference. CFSR, ERA-Interim, and MERRA capture this feature well; in fact, CFSR's high native spatial resolution provides sharp depiction of the current in the plotted specific humidity difference field. The contribution of the trailing cold front to the air-sea differences can be seen as well, particularly in ERA-Interim and MERRA. The high differences associated with the cold front are the second region of high fluxes located further into the Atlantic Ocean, away from the US coast and north of the Caribbean islands.

Combining the high air-sea specific humidity differences with the high wind speeds observed around the warm seclusion (Figure 4-22), determines where the high LHF values occur. High wind speeds are seen wrapping around the storm from along the leading cold front up around the warm occlusion and down the rear of the storm where the dry intrusion is located.

CFSR and NCEP-R2 both have similarly high wind speeds, whereas MERRA and ERA-Interim have lower wind speed magnitudes and more regionally confined maxima. The SeaFlux interpolated data set does not resolve the fronts and gradients well, and appears to poorly capture the peak wind speed magnitudes that are seen in the comparison data.

The SHF also evolves in time with the development of the warm seclusion's strength and structure in a similar manner to the LHF. During the early stages of the warm seclusion, the warm front is the key feature of the storm and the air-sea temperature differences are low, leading to low SHF values. At this time, the contribution of the western boundary current can be seen as the region of high SHF (approximately 150-200 $Wm^{-2}$) just off the US coast. As time progresses, the frontal structure develops and wraps around the system more, and the fluxes begin to increase with the increasing wind associated with the dry intrusion from the rear. By 17 November 2004 00Z, shown in Figure 4-23, the high SHF values are behind the bent-back warm front and behind the trailing cold front, tucked south of the occluded warm air. CFSR has a peak value in excess of 300 $Wm^{-2}$, SeaFlux, ERA-Interim, and NCEP-R2's peak value is around 250 $Wm^{-2}$, and MERRA's peak SHF value is approximately 170 $Wm^{-2}$ (a likely underestimation). These values are difficult to verify in the comparison data due to the gaps between the satellite swaths.

The air-sea temperature differences (Figure 4-24) appear to be a driving factor in the SHF, particularly in the spatial structure of the SHF fields. Peak values in excess of 10 K are seen in almost all the reanalysis data sets, with the exception of NCEP-R2. These high air-sea temperature differences are likely produced by the western boundary current transporting warm tropical water to the Northern latitudes. Additionally, the colder air at these higher latitudes and the comparatively cooler air associated with the cold frontal systems creates large air-sea temperature differences, priming the region for high SHF values.

This case exhibits peculiar behavior in regards to the storm related increases in the turbulent heat fluxes. Both LHF and SHF do not increase substantially from the early stages of the storm's life cycle to the mature stage. This is a consequence of the western boundary current producing a large background flux signal. Therefore, when the warm seclusion moves into the same region as boundary current, a large flux of energy is already occurring and the energy transfer resulting from the storm event does not impact the region with the same magnitudes that are seen in the other two cases.

The contribution of the fluxes from the North Atlantic warm seclusion to the monthly ocean basin flux totals are evaluated in three box and whisker analyses seen in the Figure 4-25 and Figure 4-26 for the LHF and SHF, respectively. The warm seclusion increases the mean of CFSR and SeaFlux from the non-storm analysis compared to the monthly ocean basin total integrated flux. The means of the other four data sets do not change much; however, the warm seclusion does increase the 75th and 99th percentiles for the reanalysis data sets. For the SHF box and whisker plot analyses, the changes to the 50th and other percentiles from including the warm seclusion are small. The ratios of the 50th percentile of the storm-only time-integrated flux to the 50th percentile of the monthly ocean basin total time-integrated fluxes are included in Table 4-3. The mean of the storm only time-integrated total LHF accounts for 17-21% of the mean monthly total ocean basin time-integrated total LHF for the reanalyses, but only 12.5% for the interpolated SeaFlux data set. These percentages are relevant to explaining the amount of heat flux being contributed to the monthly value as a result of this warm seclusion (recall that this system lasted for 7 of the 30 days in November; covering approximately 35% of the ocean basin). The ratio of the storm-centric mean to the monthly ocean basin total for the SHF has a broad range varying from 12% for ERA-Interim to 23% for NCEP-R2 with the interpolated SeaFlux data set, MERRA, and CFSR in between.

## 4.4 Summary of results

A few conclusions regarding the turbulent heat fluxes can be drawn from the analysis of these three warm seclusion cases. The highest fluxes arising from a warm seclusion are associated with the region behind the trailing cold and are strongest during the mature stage of the seclusion. These high flux values develop rapidly with the strengthening of the storm system, particularly with the dry intrusion and the bent-back frontal structure. Both the LHF and SHF reach values that are approximately an order of magnitude greater than the background fluxes that occur in their respective ocean basins (with the exception of the background fluxes originating from the western boundary current).

This study also shows that satellites are capable of providing reasonably accurate data that can be used to compute the turbulent heat fluxes with known uncertainties. This is primarily a result of recent advances in satellite regression techniques and retrieval methods. However, modeled and gridded reanalysis products have their applications as well. But it is imperative to

realize that the choice of data set does matter. As is seen in the three case analyses, not all reanalysis data sets are equal, and each provides differing results. For example, some data sets, such as MERRA, systematically underestimate the fluxes, whereas other data sets' performance depends on native model spatial and temporal resolution or on environmental and specific storm characteristics.

The accurate representation of warm seclusions in the data sets and flux fields is essential from flux climatology and regional energy budget perspectives. Warm seclusions are responsible for roughly one quarter of the turbulent heat fluxes occurring in a specific monthly ocean basin. These storms occupy a comparatively small subset in both space and time (around 30% of the spatial area of the ocean basin and only a few days out of the month), yet these storms account for a disproportionately large portion of the monthly fluxes.

**Table 4-1**: The ratios of the storm-centric, time-integrated total heat flux to the monthly ocean basin time-integrated total heat flux for the 50th percentile for the North Pacific warm seclusion case for both LHF and SHF.

| Warm Seclusion: North Pacific Case | | |
|---|---|---|
| Ratio of Storm-centric Time-Integrated Total Flux to Monthly Ocean Basin Time-Integrated Total Flux | | |
| | Data Set | 50th Percentile |
| LHF | CFSR | 0.132 |
| | ERA-Interim | 0.138 |
| | MERRA | 0.129 |
| | NCEP-R2 | 0.156 |
| | SeaFlux | 0.171 |
| SHF | CFSR | 0.184 |
| | ERA-Interim | 0.201 |
| | MERRA | 0.215 |
| | NCEP-R2 | 0.203 |
| | SeaFlux | 0.166 |

**Table 4-2**: The ratios of the storm-centric, time-integrated total heat flux to the monthly ocean basin time-integrated total heat flux for the 50th percentile for the South Pacific warm seclusion case for both LHF and SHF.

| Warm Seclusion: South Pacific Case | | |
|---|---|---|
| Ratio of Storm-centric Time-Integrated Total Flux to Monthly Ocean Basin Time-Integrated Total Flux | | |
| | Data Set | 50th Percentile |
| LHF | CFSR | 0.310 |
| | ERA-Interim | 0.307 |
| | MERRA | 0.299 |
| | NCEP-R2 | 0.323 |
| | SeaFlux | 0.294 |
| SHF | CFSR | 0.558 |
| | ERA-Interim | 0.431 |
| | MERRA | 0.370 |
| | NCEP-R2 | 0.786 |
| | SeaFlux | 0.476 |

**Table 4-3**: The ratios of the storm-centric, time-integrated total heat flux to the monthly ocean basin time-integrated total heat flux for the 50th percentile for the North Atlantic warm seclusion case for both LHF and SHF.

| Warm Seclusion: North Atlantic Case | | |
|---|---|---|
| Ratio of Storm-centric Time-Integrated Total Flux to Monthly Ocean Basin Time-Integrated Total Flux | | |
| | Data Set | 50th Percentile |
| LHF | CFSR | 0.210 |
| | ERA-Interim | 0.171 |
| | MERRA | 0.182 |
| | NCEP-R2 | 0.198 |
| | SeaFlux | 0.126 |
| SHF | CFSR | 0.164 |
| | ERA-Interim | 0.120 |
| | MERRA | 0.179 |
| | NCEP-R2 | 0.231 |
| | SeaFlux | 0.155 |

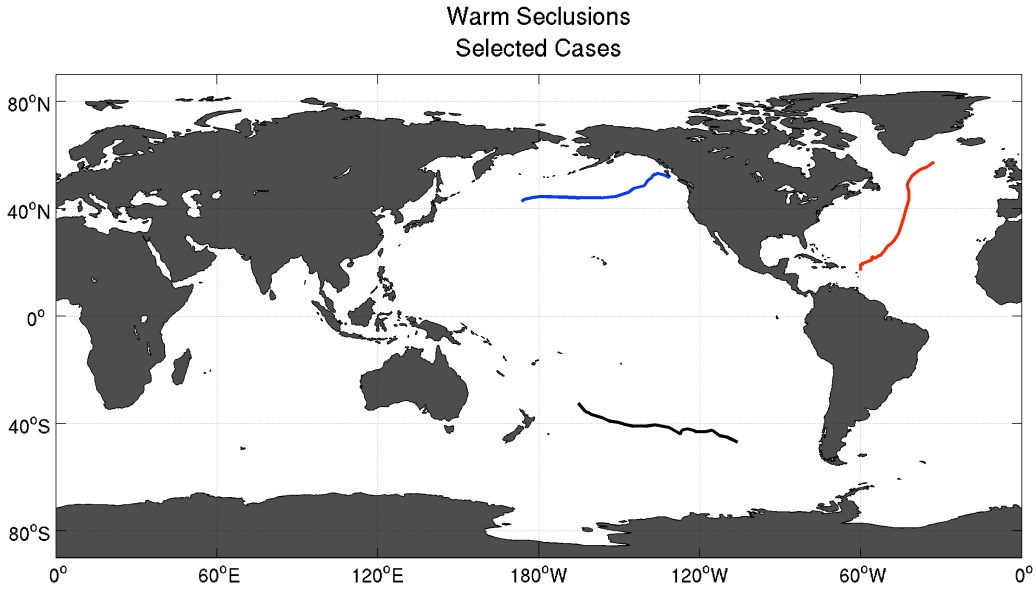


**Figure 4-1**: Track plot for the three selected warm seclusion cases, per Maue [2010]'s identification algorithm. The North Pacific case's track is in blue, lasting from 05 October 2004 to 09 October 2004; this storm traveled from west to east. The South Pacific case's track is in black lasting from 05 November 2003 to 12 November 2003; this storm traveled from west to east. The North Atlantic case's track is in red lasting from 13 November 2004 to 20 November 2004; this storm traveled from south to north.

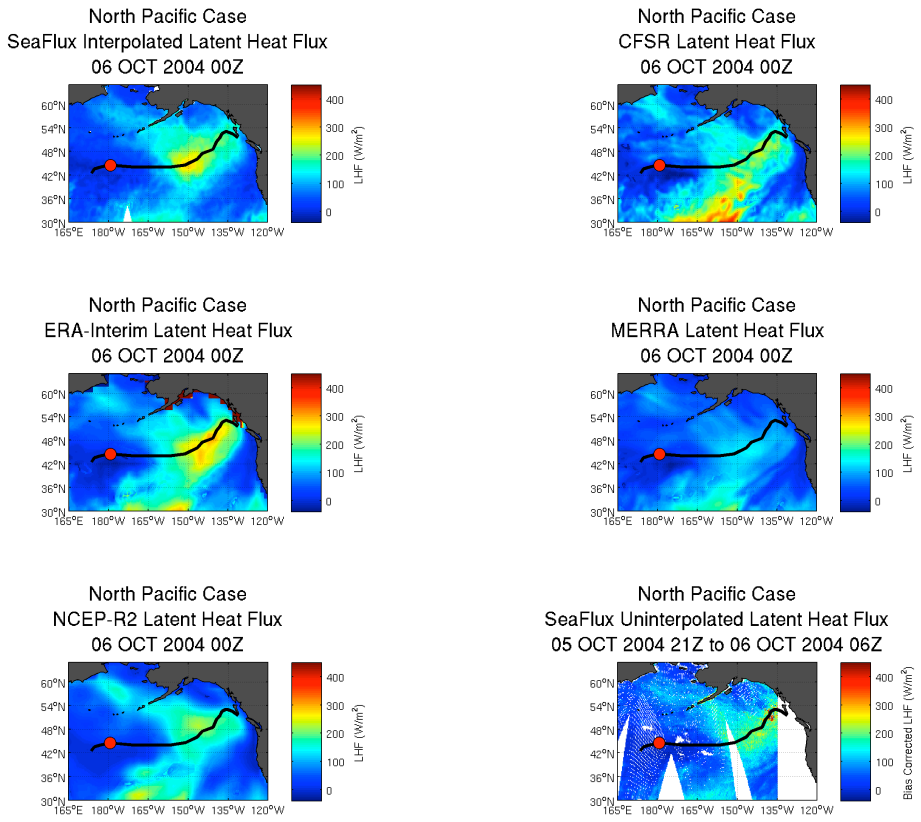


**Figure 4-2**: The LHF for the North Pacific case for a fixed point in time, 06 October 2004 valid for 00Z. The sixth panel contains the bias-corrected LHF comparison data from the SeaFlux uninterpolated swath data. The black line indicates the track of the warm seclusion from Maue [2010]'s algorithm. The red dot indicates the center of the warm seclusion.

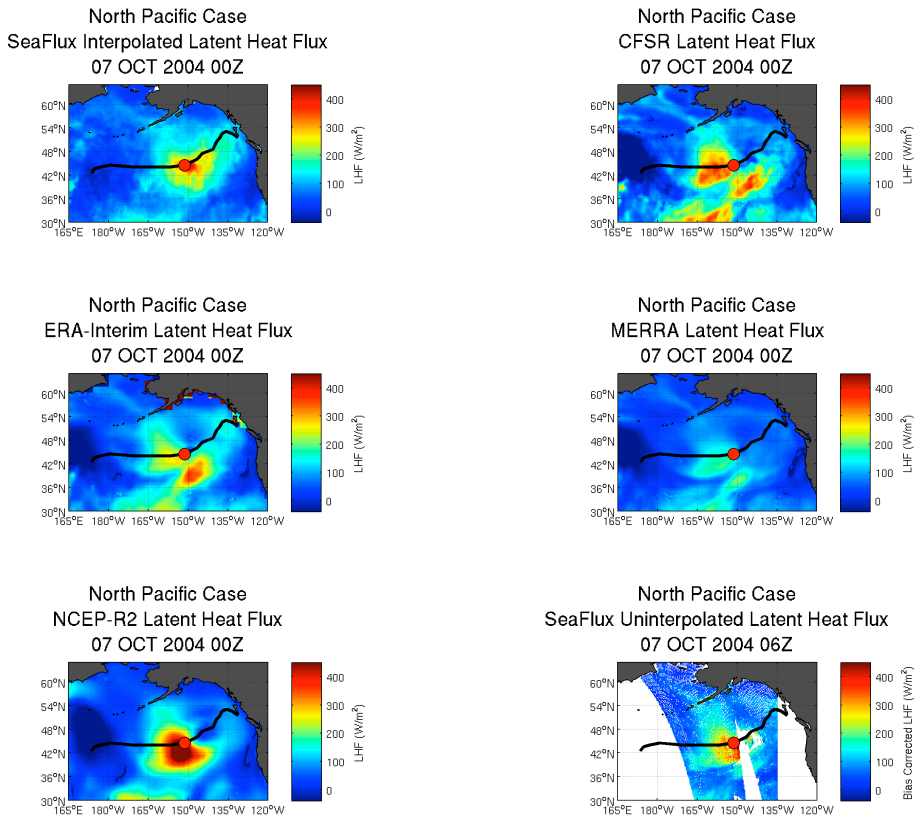


**Figure 4-3**: The LHF for the North Pacific case for a fixed point in time, 07 October 2004 valid for 00Z. The sixth panel contains the bias-corrected LHF comparison data from the SeaFlux uninterpolated swath data. The black line indicates the track of the warm seclusion from Maue [2010]'s algorithm. The red dot indicates the center of the warm seclusion.

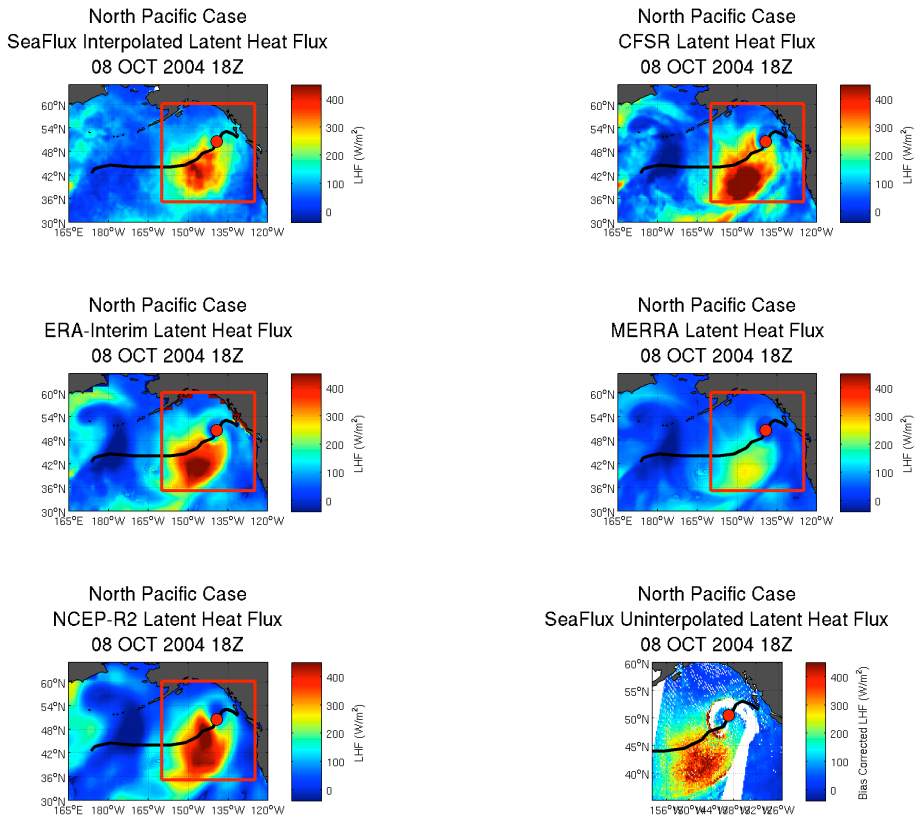


**Figure 4-4**: The LHF for the North Pacific case for a fixed point in time, 08 October 2004 valid for 18Z. The sixth panel contains the bias-corrected LHF comparison data from the SeaFlux uninterpolated swath data. The domain of the SeaFlux uninterpolated swath comparison data is indicated by the red box. The black line indicates the track of the warm seclusion from Maue [2010]'s algorithm. The red dot indicates the center of the warm seclusion.

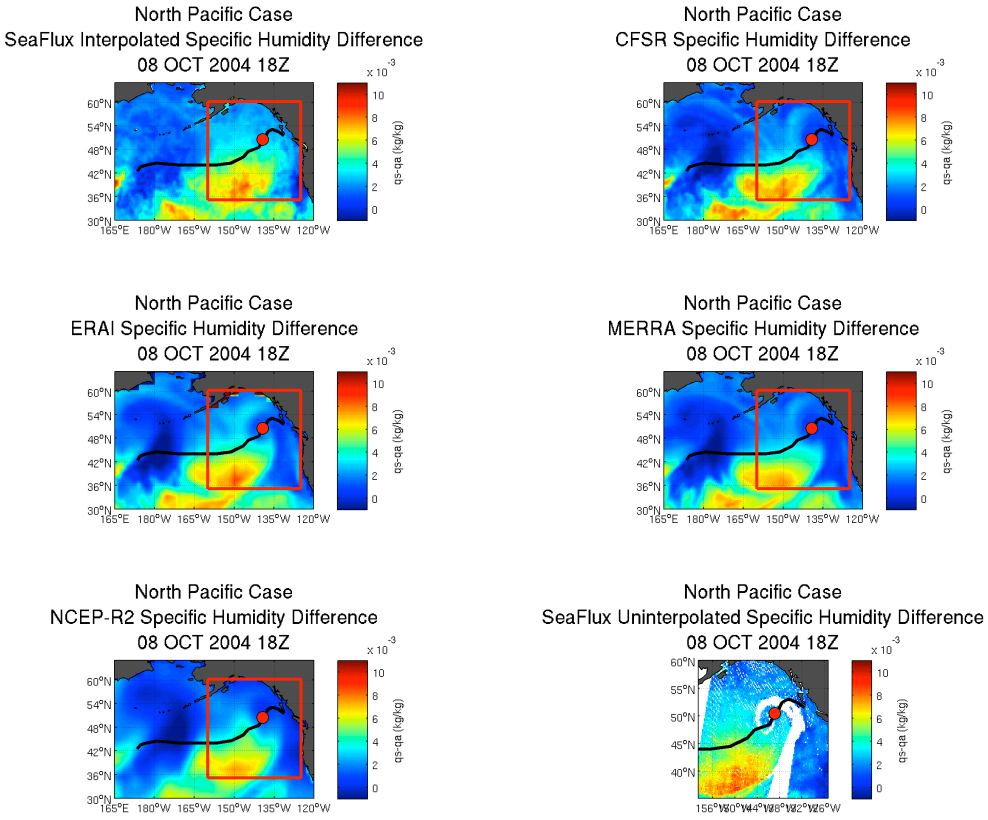


**Figure 4-5**: The air-surface specific humidity differences for the North Pacific case for a fixed point in time, 08 October 2004 valid for 18Z. The sixth panel contains the bias-corrected specific humidity difference comparison data. The domain of the SeaFlux uninterpolated swath comparison data is indicated by the red box. The black line indicates the track of the warm seclusion from Maue [2010]'s algorithm. The red dot indicates the center of the warm seclusion.

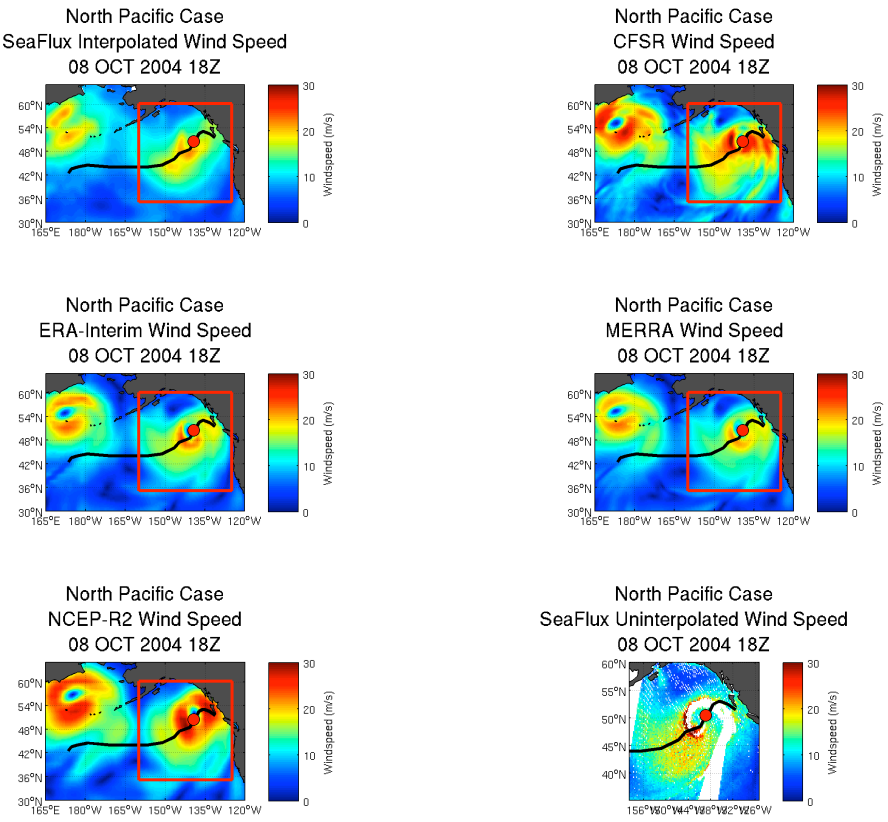


**Figure 4-6**: The wind speed for the North Pacific case for a fixed point in time, 08 October 2004 valid for 18Z. The sixth panel contains the bias-corrected wind speed comparison data. The domain of the SeaFlux uninterpolated swath comparison data is indicated by the red box. The black line indicates the track of the warm seclusion from Maue [2010]'s algorithm. The red dot indicates the center of the warm seclusion.

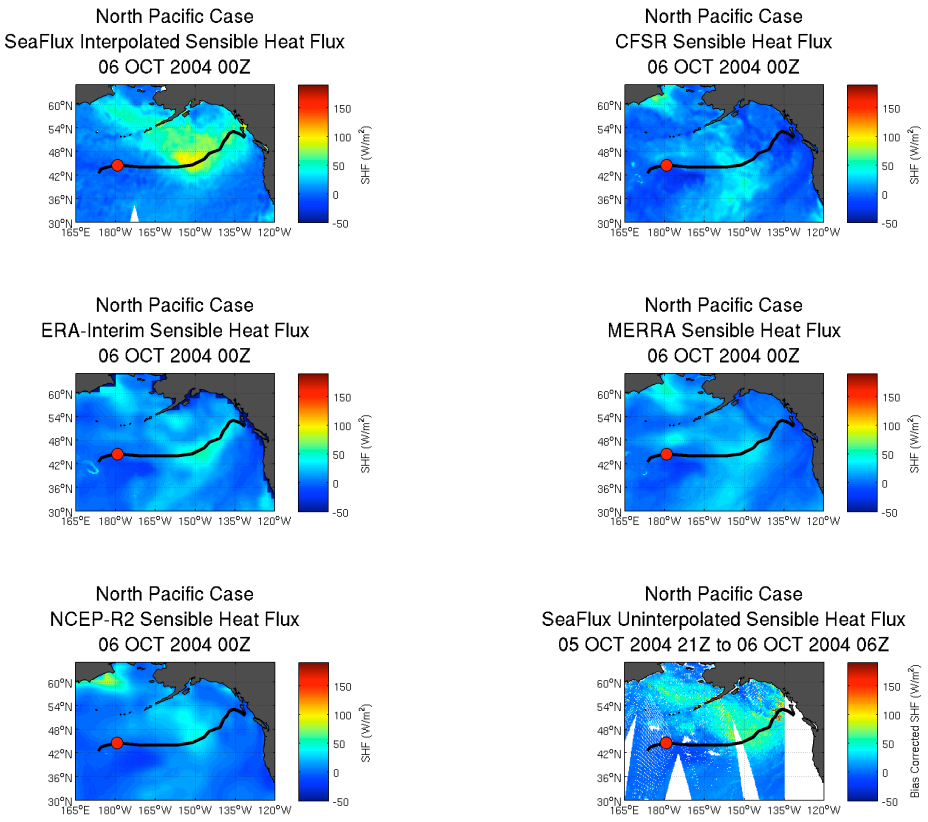


**Figure 4-7**: The SHF for the North Pacific case for a fixed point in time, 08 October 2004 valid for 18Z. The sixth panel contains the bias-corrected SHF comparison data. The black line indicates the track of the warm seclusion from Maue [2010]'s algorithm. The red dot indicates the center of the warm seclusion.

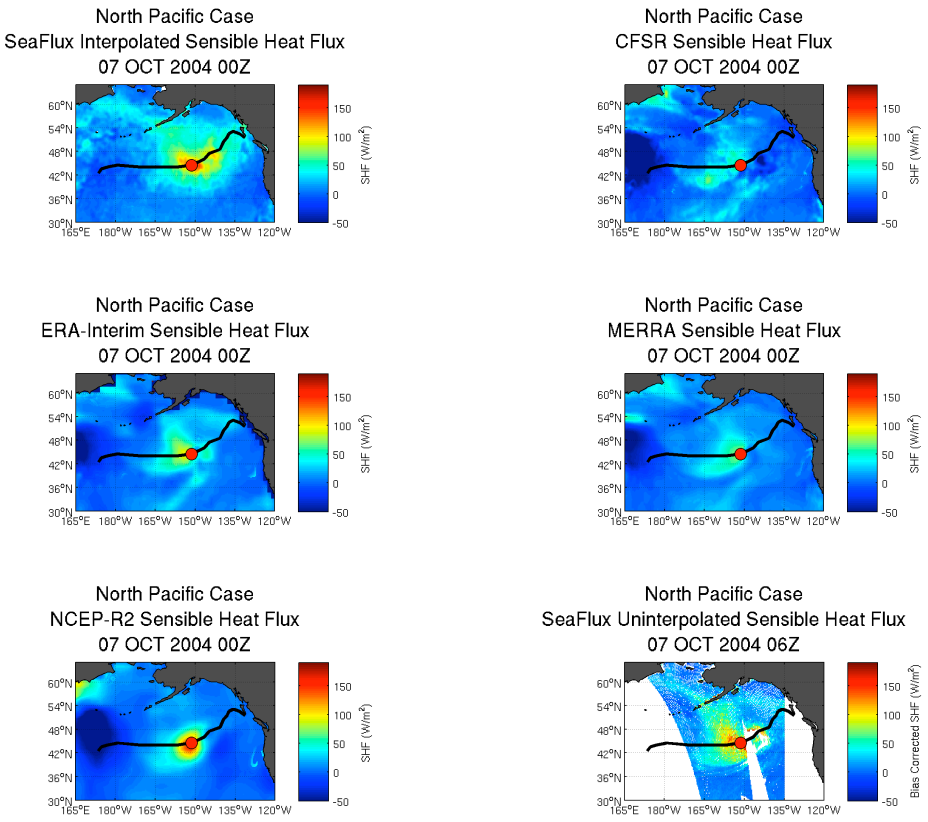


**Figure 4-8**: The SHF for the North Pacific case for a fixed point in time, 08 October 2004 valid for 18Z. The sixth panel contains the bias-corrected SHF comparison data. The black line indicates the track of the warm seclusion from Maue [2010]'s algorithm. The red dot indicates the center of the warm seclusion.

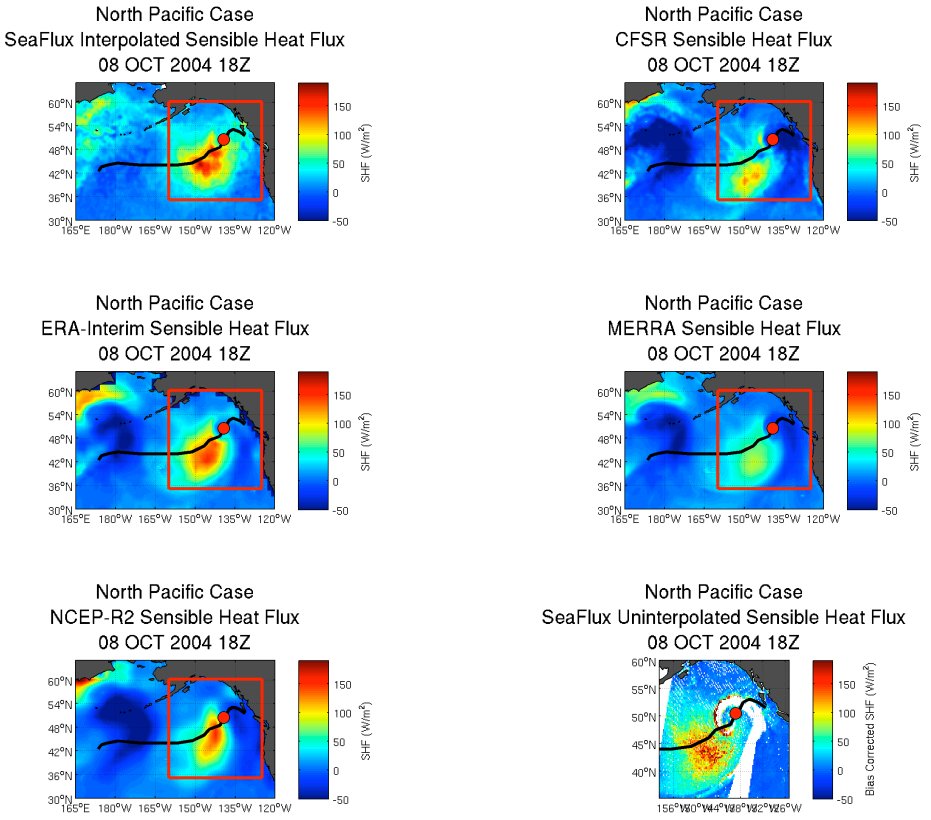


**Figure 4-9**: The SHF for the North Pacific case for a fixed point in time, 08 October 2004 valid for 18Z. The sixth panel contains the bias-corrected SHF comparison data. The domain of the SeaFlux uninterpolated swath comparison data is indicated by the red box. The black line indicates the track of the warm seclusion from Maue [2010]'s algorithm. The red dot indicates the center of the warm seclusion.

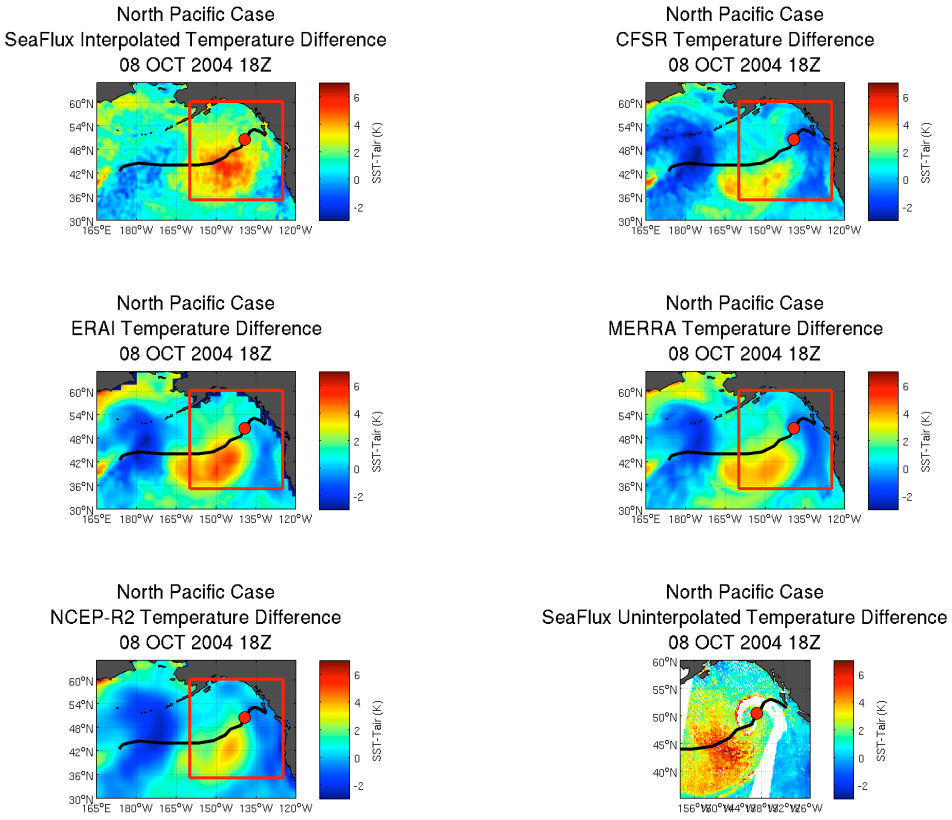


**Figure 4-10**: The air-sea temperature differences for the North Pacific case for a fixed point in time, 08 October 2004 valid for 18Z. The sixth panel contains the bias-corrected temperature difference comparison data. The domain of the SeaFlux uninterpolated swath comparison data is indicated by the red box. The black line indicates the track of the warm seclusion from Maue [2010]'s algorithm. The red dot indicates the center of the warm seclusion.

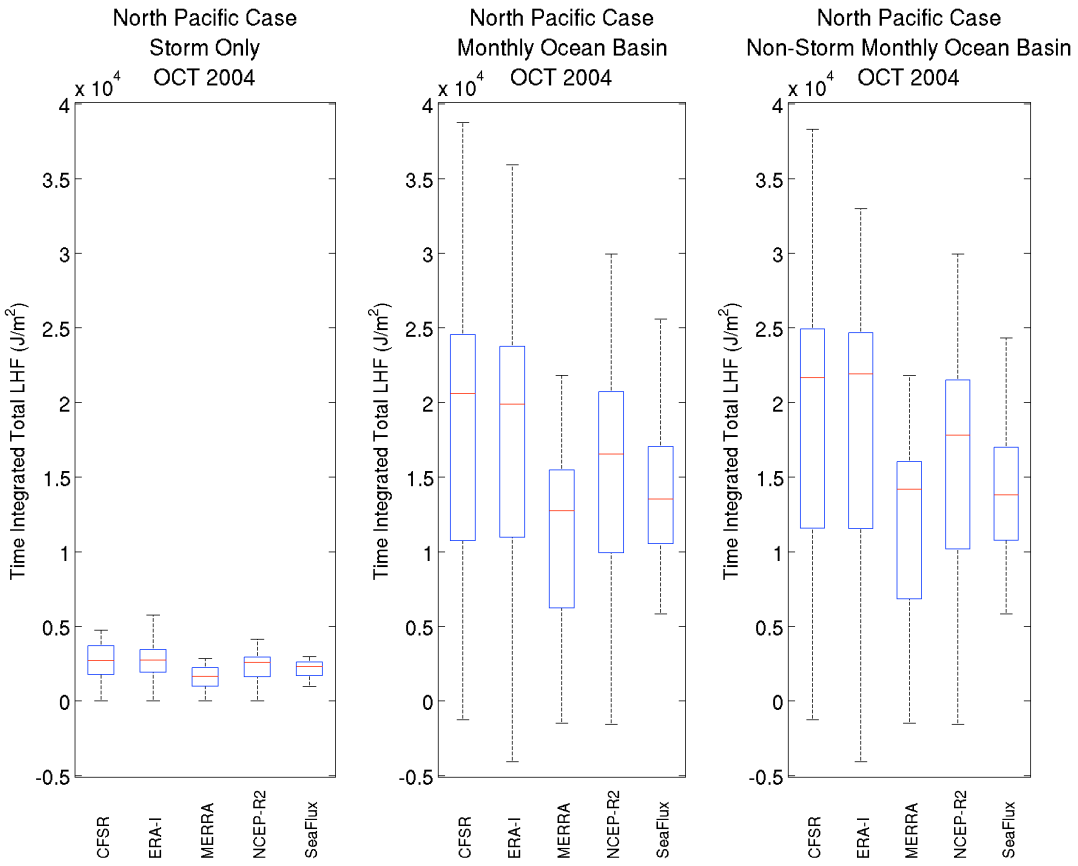


**Figure 4-11**: The total time-integrated LHF for the storm-centric, event-only analysis (first panel); the total time-integrated LHF for the total monthly ocean basin (second panel); the total time-integrated LHF for the total monthly ocean basin without the warm seclusion (third panel). The lowest whisker marks the 1st percentile, the bottom of the box represents the 25th percentile, the bar represents the mean, the top of the box represents the 75th percentile, and the upper whisker marks the 99th percentile.

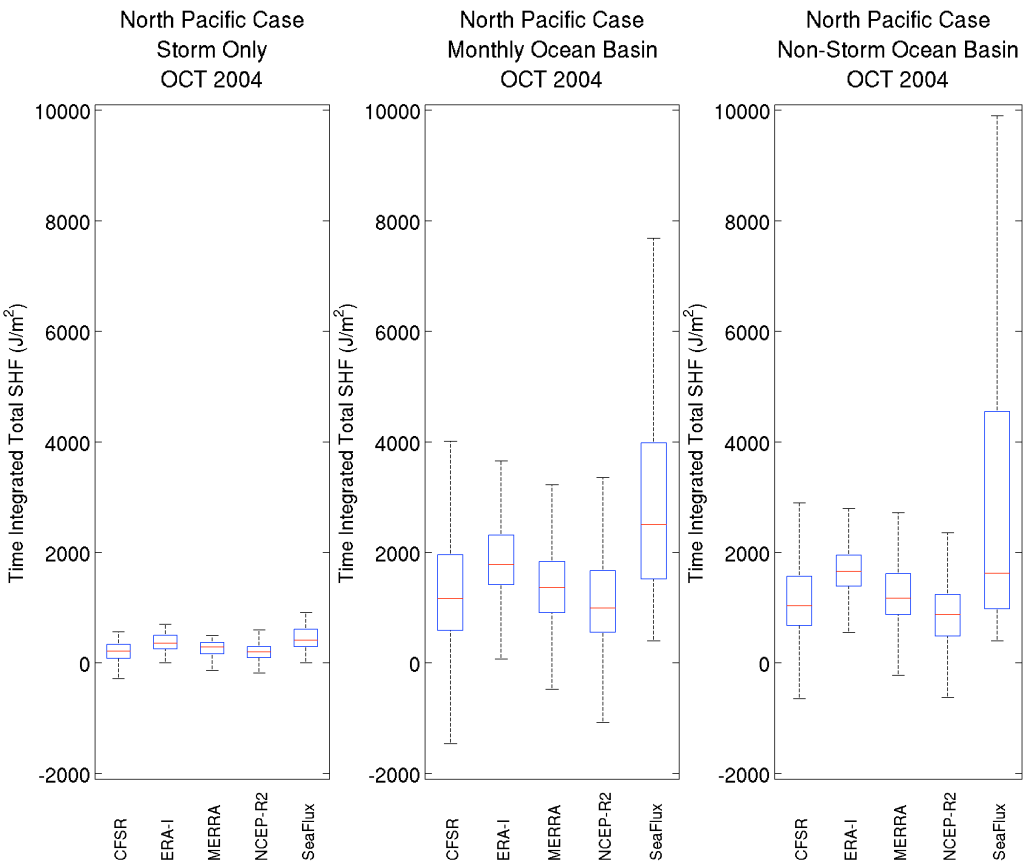


**Figure 4-12**: Same as Figure 4-11 but for SHF.

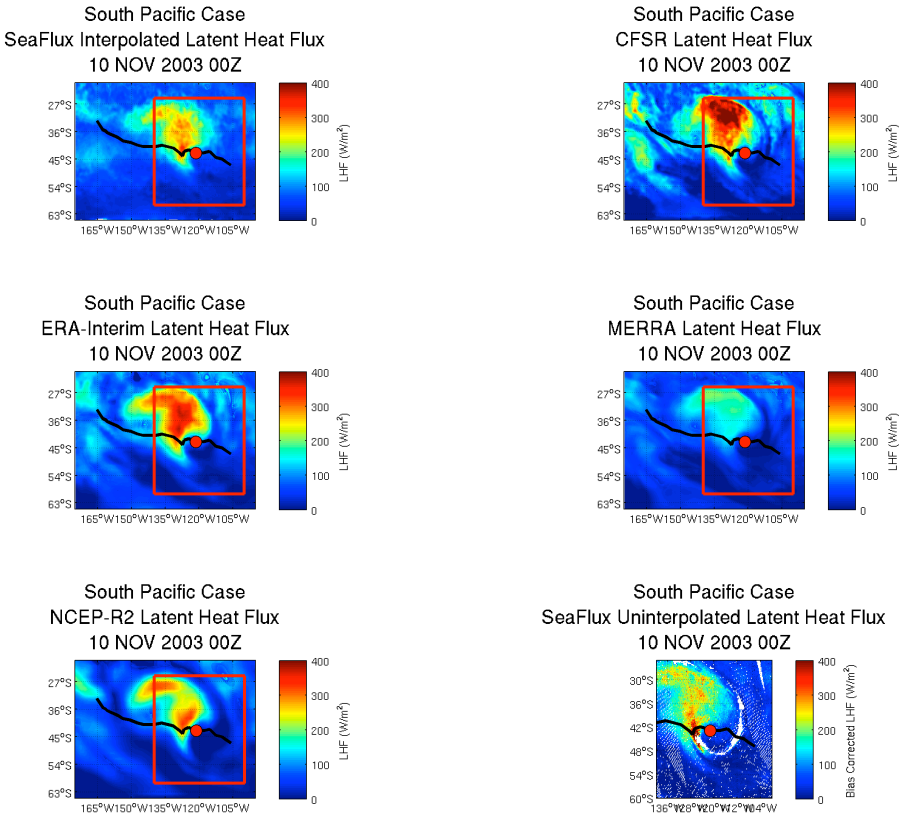


**Figure 4-13**: The LHF for the South Pacific case for a fixed point in time, 10 November 2003 valid for 00Z. The sixth panel contains the bias-corrected LHF comparison data. The domain of the SeaFlux uninterpolated swath comparison data is indicated by the red box. The black line indicates the track of the warm seclusion from Maue [2010]'s algorithm. The red dot indicates the center of the warm seclusion.

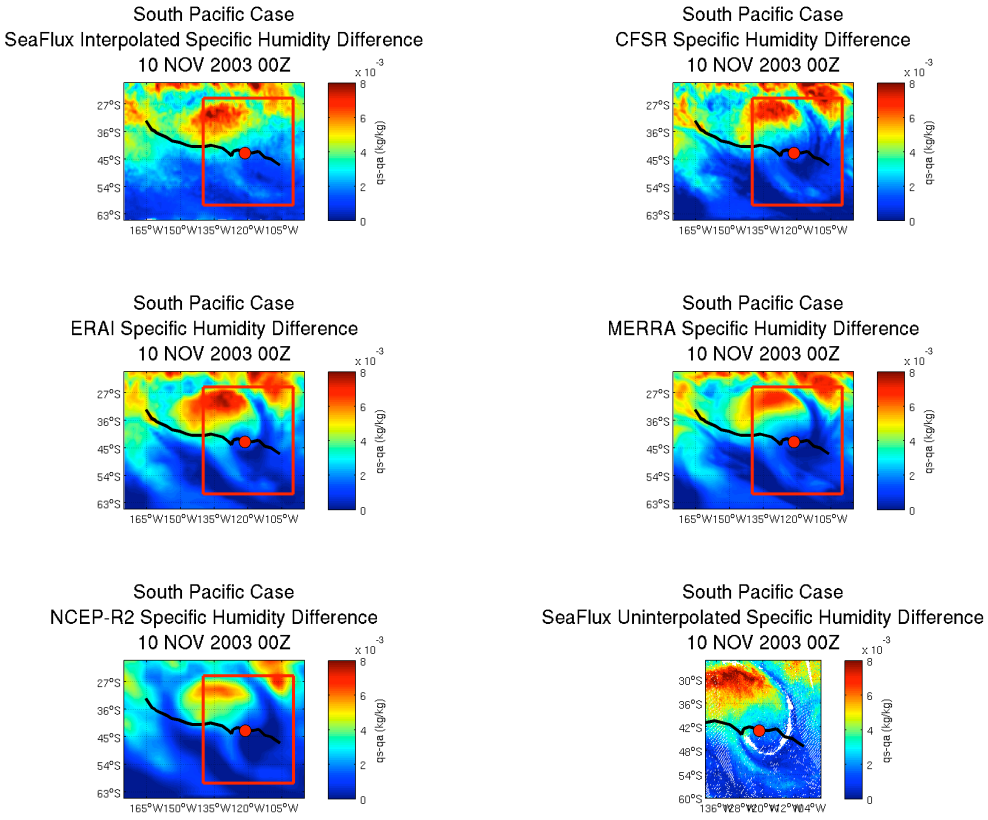


**Figure 4-14**: The air-surface specific humidity differences for the South Pacific case for a fixed point in time, 10 November 2003 valid for 00Z. The sixth panel contains the bias-corrected specific humidity difference comparison data. The domain of the SeaFlux uninterpolated swath comparison data is indicated by the red box. The black line indicates the track of the warm seclusion from Maue [2010]'s algorithm. The red dot indicates the center of the warm seclusion.

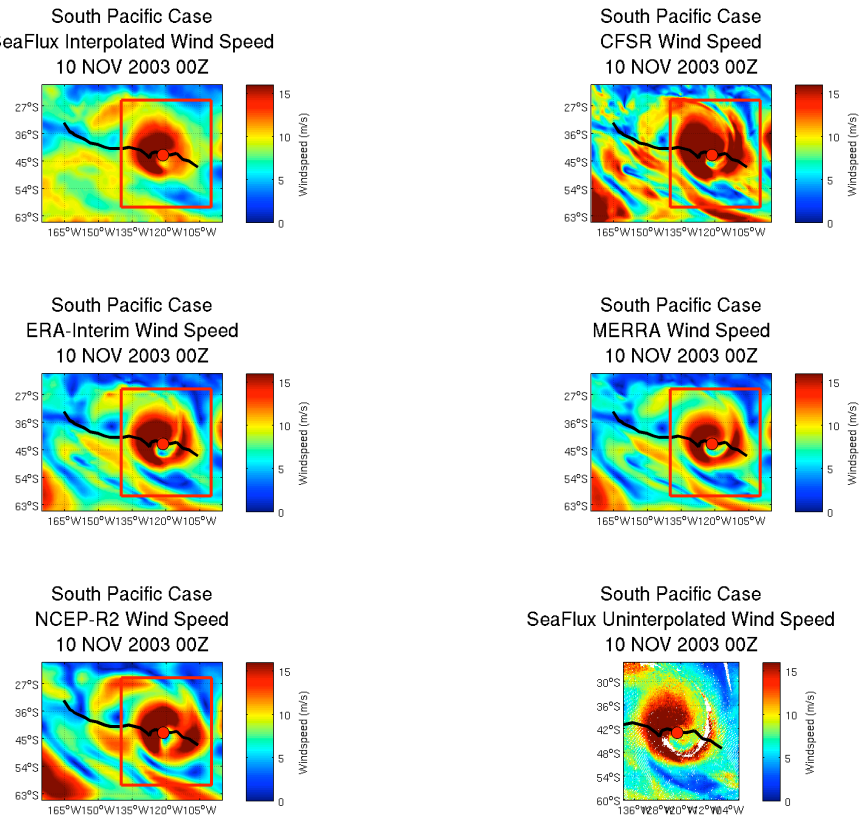


**Figure 4-15**: The wind speed for the South Pacific case for a fixed point in time, 10 November 2003 valid for 00Z. The sixth panel contains the bias-corrected wind speed comparison data. The domain of the SeaFlux uninterpolated swath comparison data is indicated by the red box. The black line indicates the track of the warm seclusion from Maue [2010]'s algorithm. The red dot indicates the center of the warm seclusion.

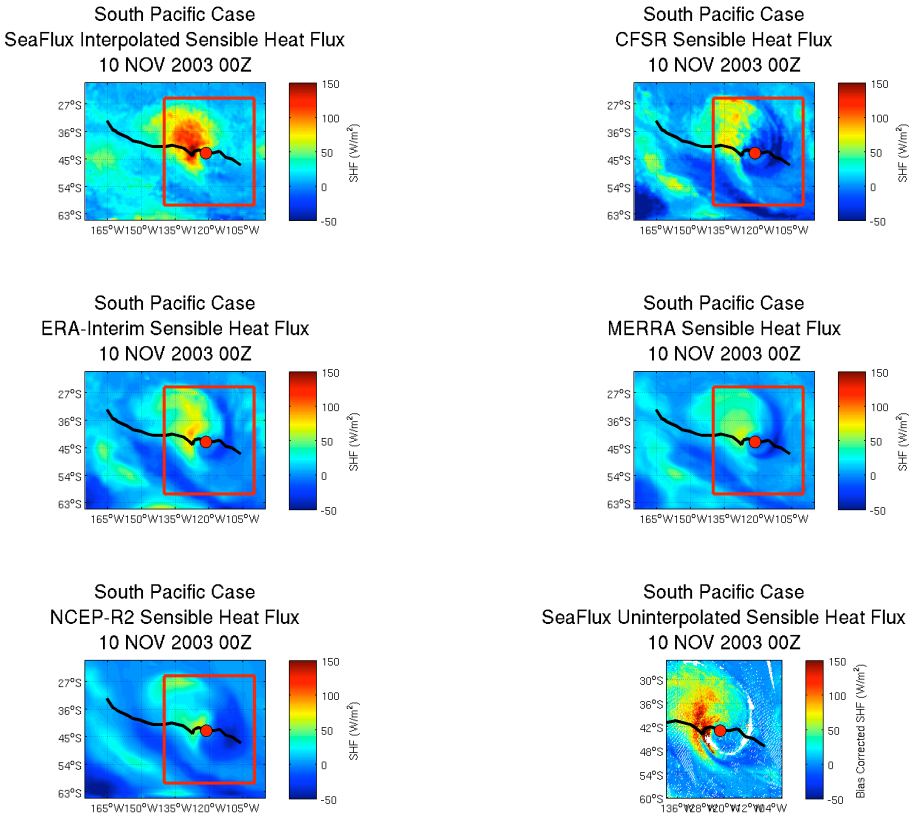


**Figure 4-16**: The SHF for the South Pacific case for a fixed point in time, 10 November 2003 valid for 00Z. The sixth panel contains the bias-corrected SHF comparison data. The domain of the SeaFlux uninterpolated swath comparison data is indicated by the red box. The black line indicates the track of the warm seclusion from Maue [2010]'s algorithm. The red dot indicates the center of the warm seclusion.

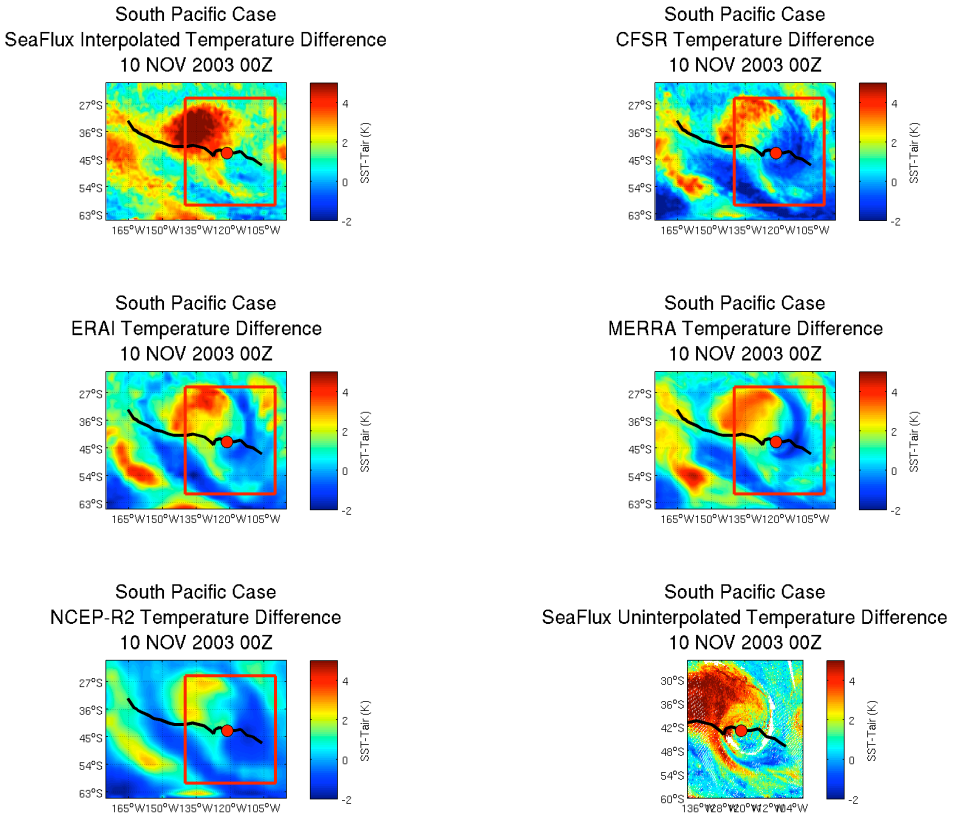


**Figure 4-17**: The air-sea temperature differences for the South Pacific case for a fixed point in time, 10 November 2003 valid for 00Z. The sixth panel contains the bias-corrected temperature difference comparison data. The domain of the SeaFlux uninterpolated swath comparison data is indicated by the red box. The black line indicates the track of the warm seclusion from Maue [2010]'s algorithm. The red dot indicates the center of the warm seclusion.

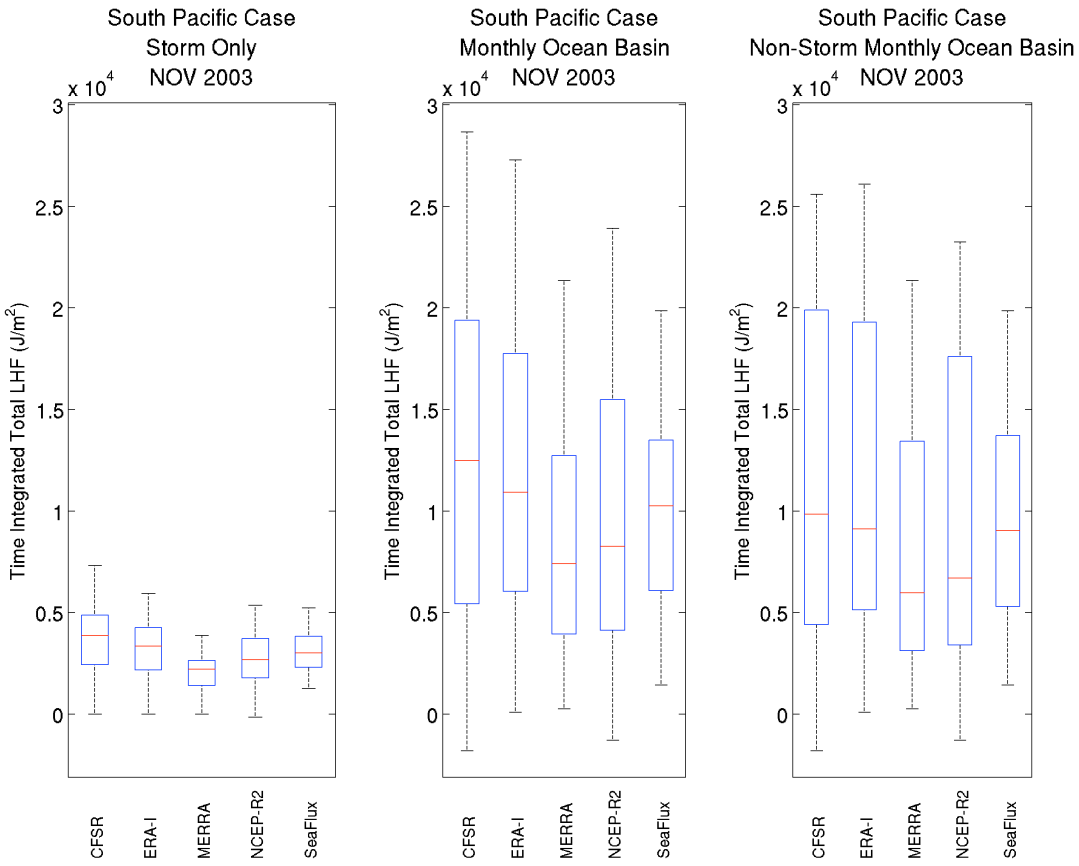


**Figure 4-18**: The total time-integrated LHF for the storm-centric, event-only analysis (first panel); the total time-integrated LHF for the total monthly ocean basin (second panel); the total time-integrated LHF for the total monthly ocean basin without the warm seclusion (third panel). The lowest whisker marks the 1st percentile, the bottom of the box represents the 25th percentile, the bar represents the mean, the top of the box represents the 75th percentile, and the upper whisker marks the 99th percentile.

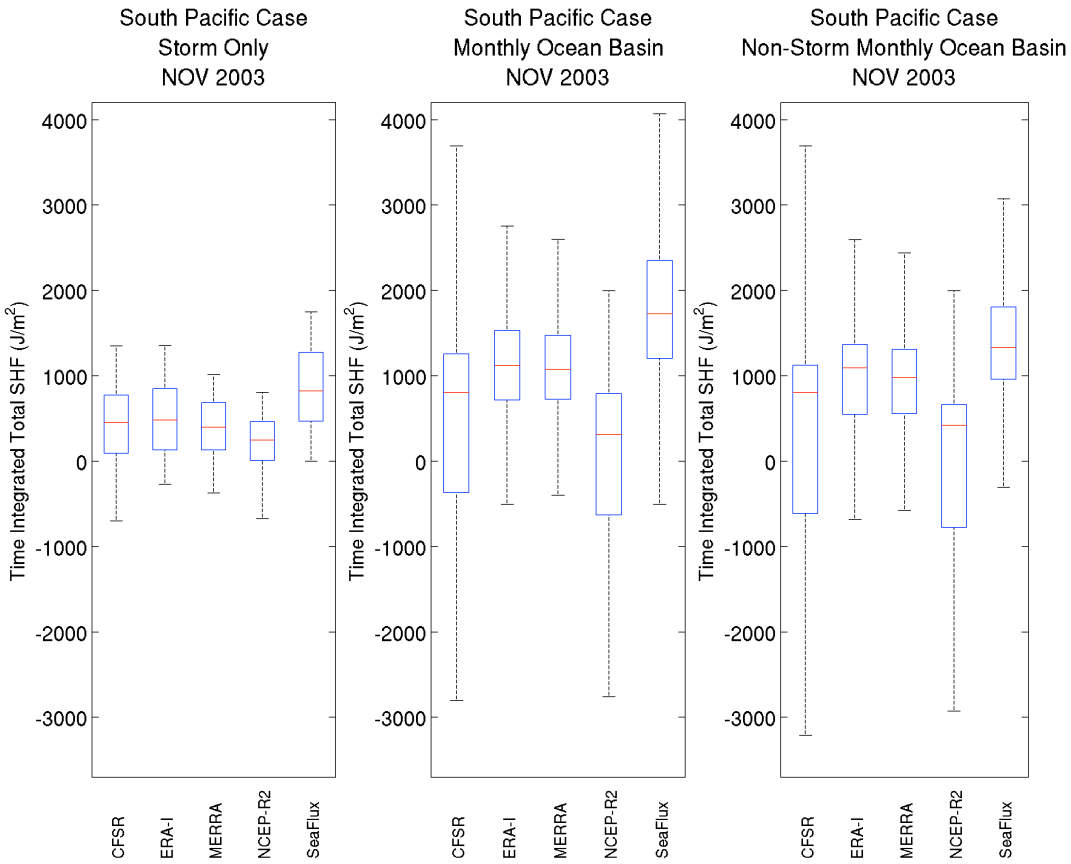


**Figure 4-19**: Same as Figure 4-18 but for SHF.

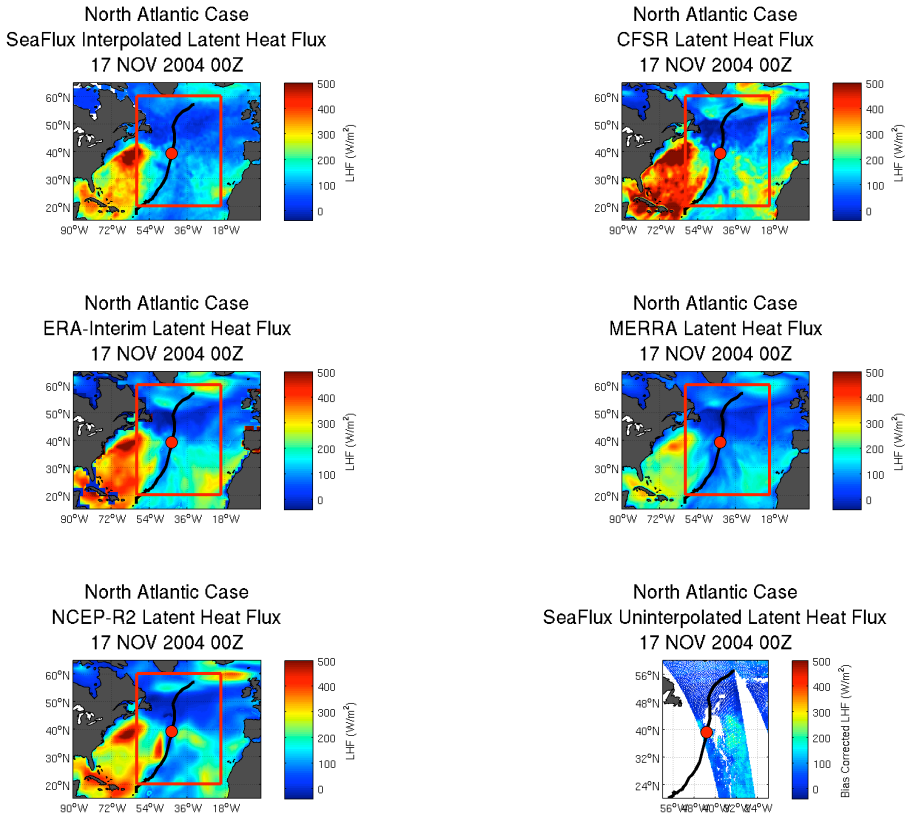


**Figure 4-20**: The LHF for the North Atlantic case for a fixed point in time, 17 November 2004 valid for 00Z. The sixth panel contains the bias-corrected LHF comparison data. The domain of the SeaFlux uninterpolated swath comparison data is indicated by the red box. The black line indicates the track of the warm seclusion from Maue [2010]'s algorithm. The red dot indicates the center of the warm seclusion.

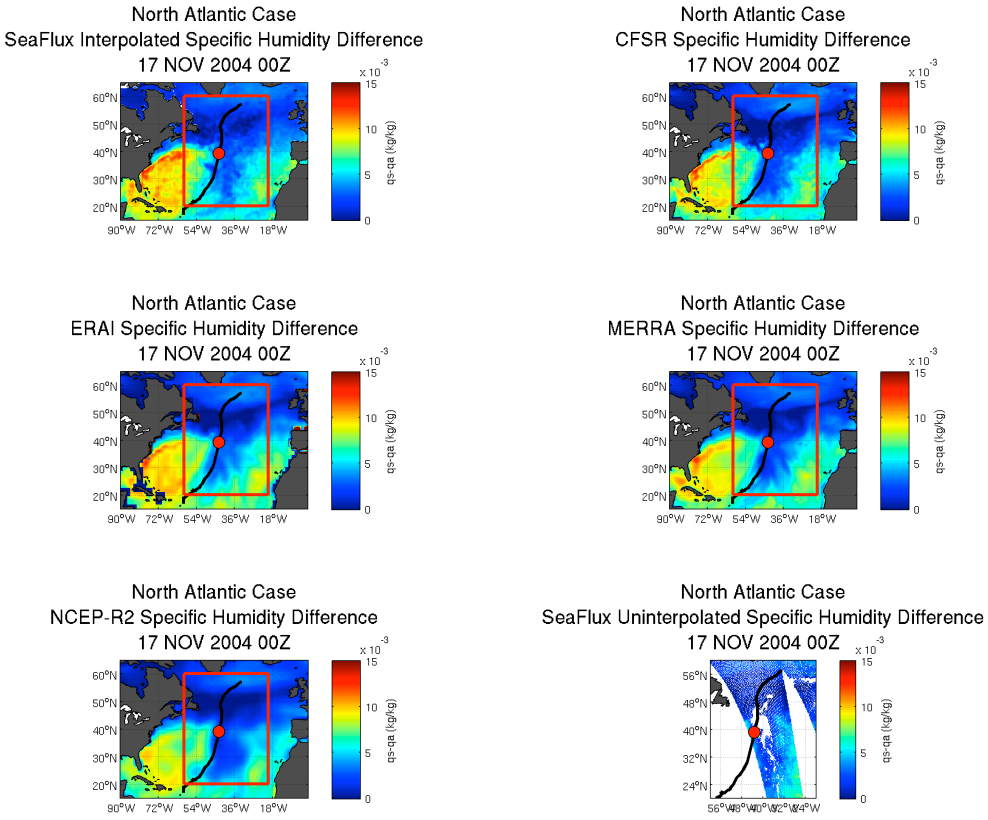


**Figure 4-21**: The air-surface specific humidity difference for the North Atlantic case for a fixed point in time, 17 November 2004 valid for 00Z. The sixth panel contains the bias-corrected specific humidity difference comparison data. The domain of the SeaFlux uninterpolated swath comparison data is indicated by the red box. The black line indicates the track of the warm seclusion from Maue [2010]'s algorithm. The red dot indicates the center of the warm seclusion.

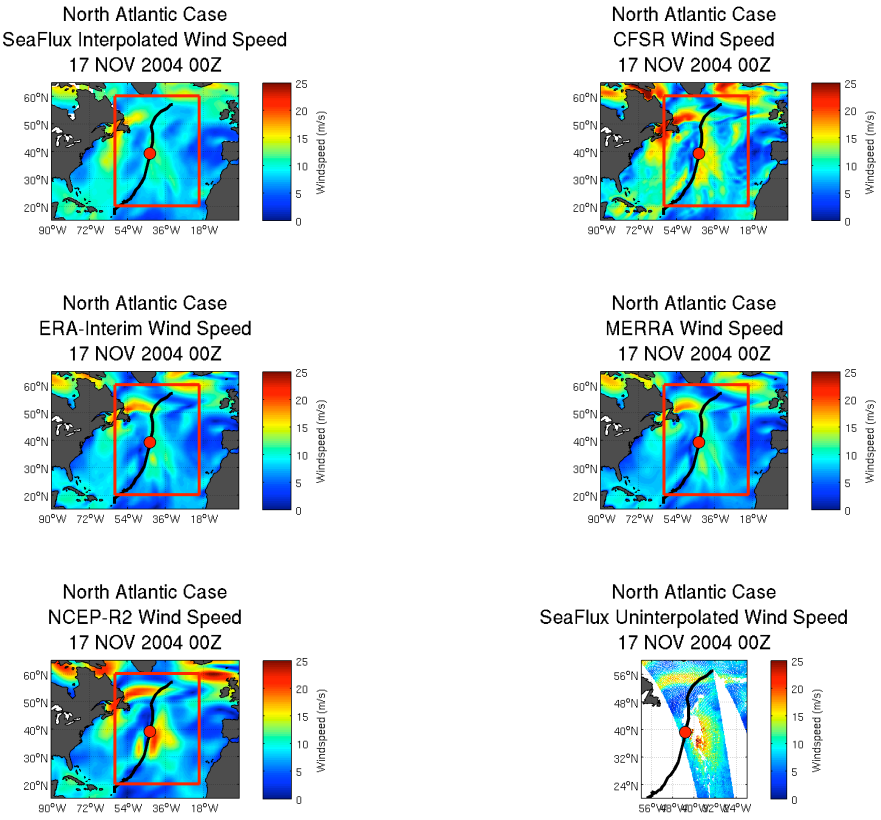


**Figure 4-22**: The wind speed for the North Atlantic case for a fixed point in time, 17 November 2004 valid for 00Z. The sixth panel contains the bias-corrected wind speed comparison data. The domain of the SeaFlux uninterpolated swath comparison data is indicated by the red box. The black line indicates the track of the warm seclusion from Maue [2010]'s algorithm. The red dot indicates the center of the warm seclusion.

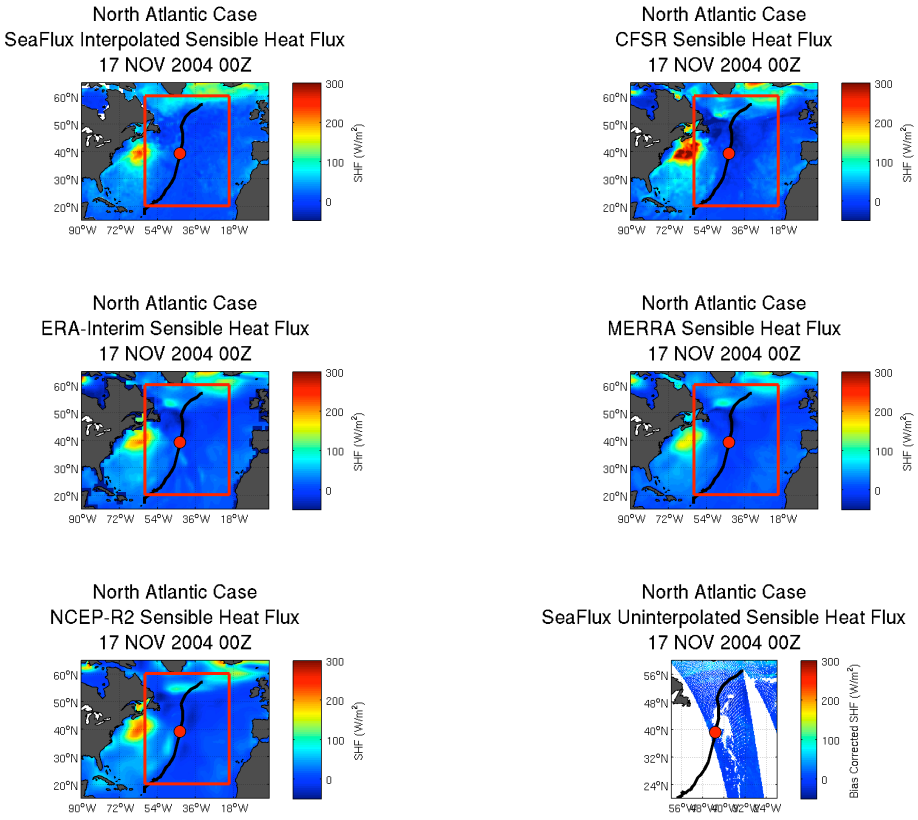


**Figure 4-23**: The SHF for the North Atlantic case for a fixed point in time, 17 November 2004 valid for 00Z. The sixth panel contains the bias-corrected SHF comparison data. The domain of the SeaFlux uninterpolated swath comparison data is indicated by the red box. The black line indicates the track of the warm seclusion from Maue [2010]'s algorithm. The red dot indicates the center of the warm seclusion.

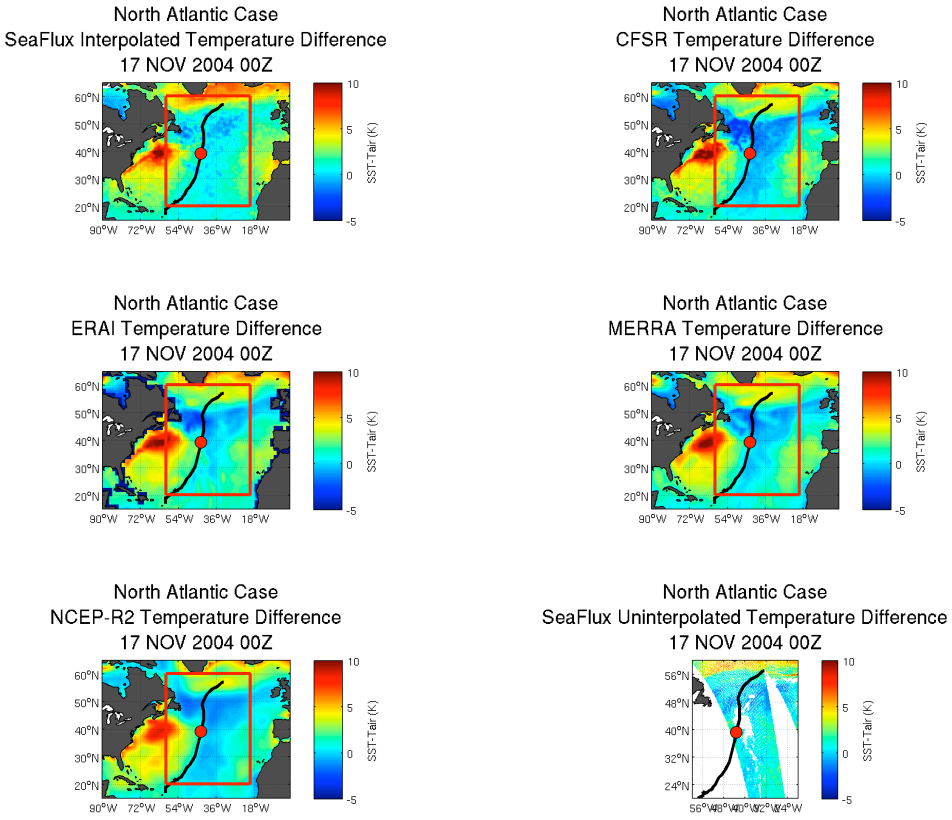


**Figure 4-24**: The air-sea temperature differences for the North Atlantic case for a fixed point in time, 17 November 2004 valid for 00Z. The sixth panel contains the bias-corrected temperature difference comparison data. The domain of the SeaFlux uninterpolated swath comparison data is indicated by the red box. The black line indicates the track of the warm seclusion from Maue [2010]'s algorithm. The red dot indicates the center of the warm seclusion.

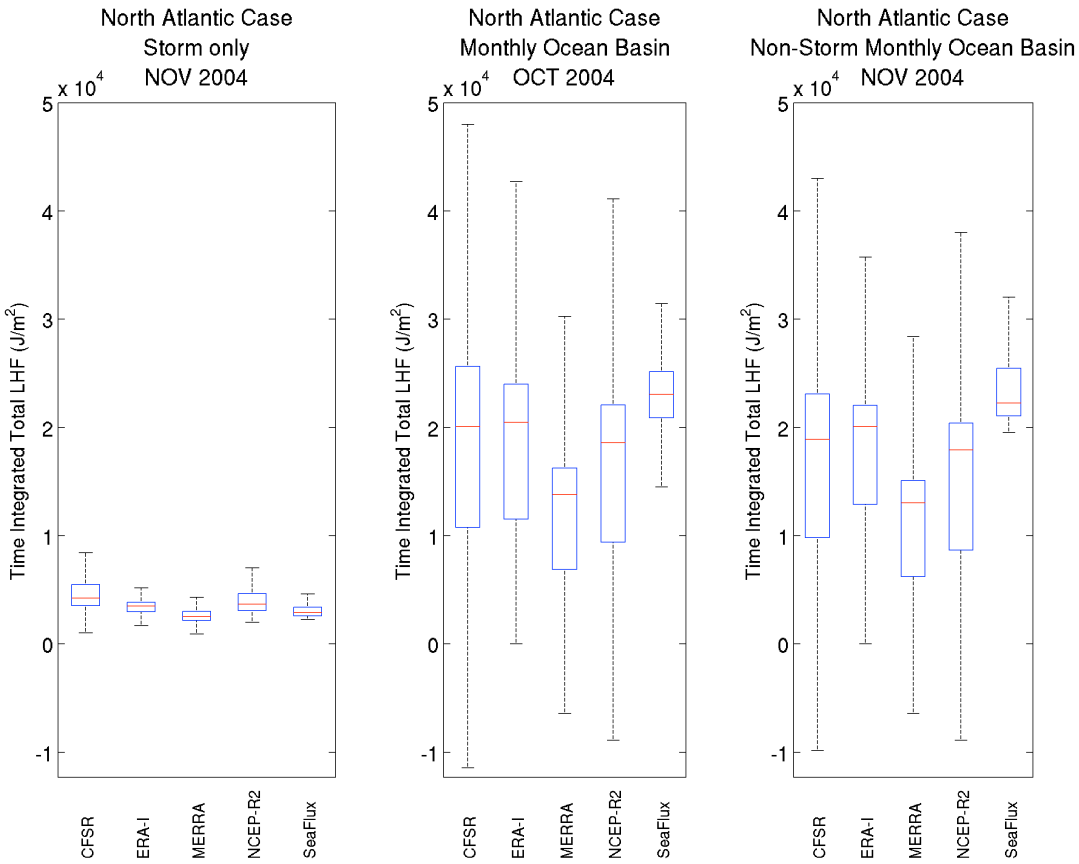


**Figure 4-25**: The total time-integrated LHF for the storm-centric, event-only analysis (first panel); the total time-integrated LHF for the total monthly ocean basin (second panel); the total time-integrated LHF for the total monthly ocean basin without the warm seclusion (third panel). The lowest whisker marks the 1st percentile, the bottom of the box represents the 25th percentile, the bar represents the mean, the top of the box represents the 75th percentile, and the upper whisker marks the 99th percentile.

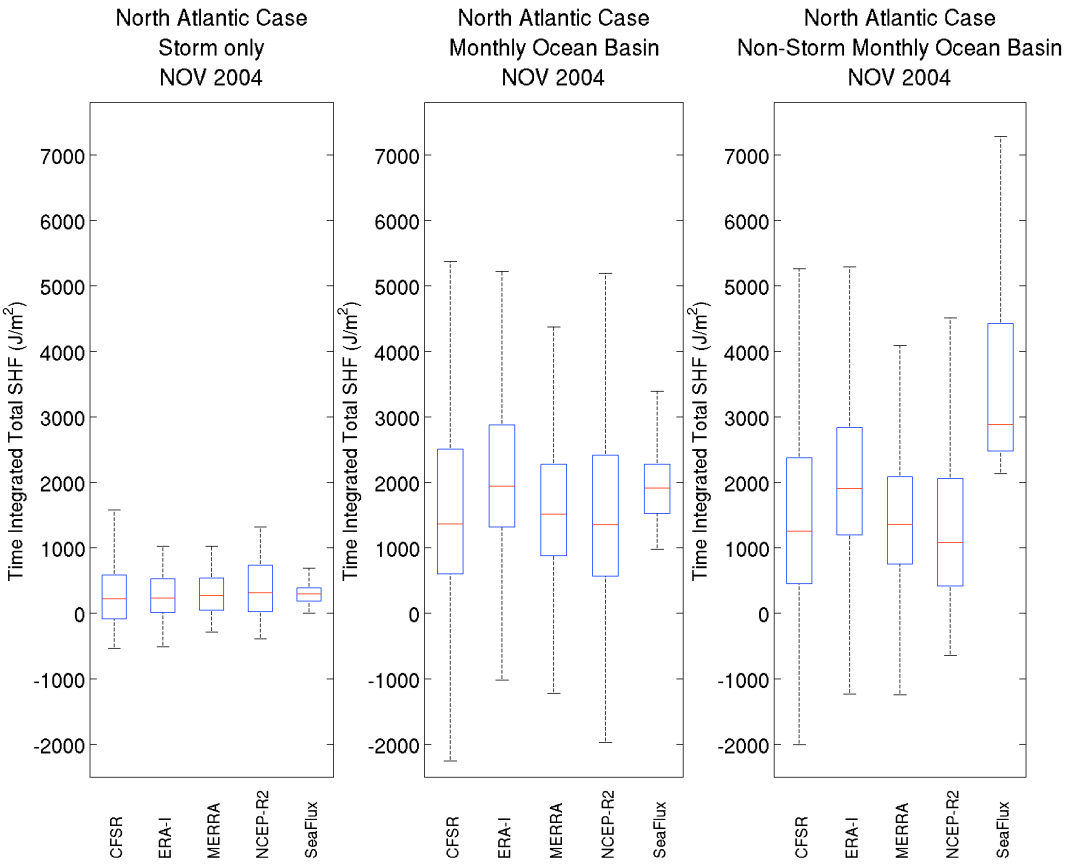


**Figure 4-26**: Same as Figure 4-25 but for SHF.

# CHAPTER FIVE

# SUMMARY

The contribution of large midlatitude storms to the turbulent heat fluxes in multiple ocean basins was evaluated for three storms. A flux computation tool, termed the modularized flux testbed (MFT), was implemented to compute the fluxes in a physically consistent manner from input component variables. The SeaFlux v0.75 data set was modified to reduce the biases associated with the input data to the flux algorithm and provide a comparison data set. These fluxes were used to conduct an evaluation of the representation warm seclusions in gridded flux products based on reanalyses and a satellite derived product. .

The satellite-derived input data used in this study were from the SeaFlux version 0.75 data sets, including both fully gridded, interpolated data and uninterpolated swath data. Multiple reanalysis data sets were also used, both well-studied data sets and newer, less well known reanalyses. The reanalysis data sets included were CFSR, ERA-Interim, MERRA, and NCEP-R2. All six data sets, both satellite and reanalysis, were used as inputs to the MFT. LHF and SHF fields were derived for each data set. This type of turbulent heat flux analysis for warm seclusions had not been previously conducted and the influence of these storms on the heat fluxes was largely unknown. This study shows the magnitude and spatial organization of the fluxes associated with different developmental stages for warm seclusions, and a general idea of the contribution these storms may have to regional energy budgets.

Warm seclusions are known for strong winds and significant spatial size. These storms typically last around three to seven days and are capable of having a sizable impact on the fluxes for that region during their lifetime. Specific values for each warm seclusion case vary but for an instantaneous snapshot of the warm seclusion in time, the peak LHF associated with the storm (during the mature phase) was between 300 and 400 $Wm^{-2}$ and the peak SHF was between 150 and 200 $Wm^{-2}$. The region of greatest fluxes was located behind the trailing cold front of the system.

To estimate the contribution of warm seclusions on the energy budget, a time integration of the total heat flux was conducted on varying domains. Three domains were considered: a

storm-centric domain, a monthly ocean basin domain, and a monthly ocean basin domain with the storm-centric domain removed. This enabled the comparison of the fluxes associated with the storm to the total flux in the ocean basin. This study found that the warm seclusion events accounted for approximately one-fourth of the total time-integrated LHF for a month in that ocean basin. These three cases also indicated that warm seclusion events may be responsible for one-fourth to one-third of the total time-integrated SHF for an ocean basin during a month, while occupying a disproportionately smaller subset in both space and time compared to the monthly ocean basin itself.

These fractions are an estimate because of the small sample size of storms under consideration. Stronger storms with higher winds and greater air-sea temperature and specific humidity differences will have higher turbulent fluxes, and weaker storms will have weaker fluxes. The duration of a warm seclusion will also impact the magnitude of the time-integrated fluxes associated with a specific storm. A climatology of warm seclusion activity is needed to further determine the comparative size and energy budget contribution of these large midlatitude storms, but a preliminary estimate of the flux impact of these storms has been established. However, with over 460 storms occurring in roughly a 3 year period, there is likely to be a sizeable integrated impact from these type of storm systems.

# REFERENCES


Andreas, E. L. (2004), Spray Stress Revisited, *J. Phys. Ocea.,* 34 (6), 1429, doi/abs/10.1175/1520-0485(2004)034<1429:SSR>2.0.CO;2.

—, E. L., P. O. G. Persson, J. E. Hare (2008), A Bulk Turbulent Air–Sea Flux Algorithm for High-Wind, Spray Conditions, *J. Phys. Ocean.,* 38 (7), 1581-1596, doi/abs/10.1175/2007JPO3813.1.

Anwender, D., P. A. Harr, and S. C. Jones (2008), Predictability associated with the downstream impacts of the extratropical transition of tropical cyclones: Case studies, *Mon. Wea. Rev*., 136, 3226-3247.

Bentamy, A., K. B. Katsaros, A. M. Mestas-Nuñoz, W. M. Drennan, E. B. Forde, and H. Roquet (2003), Satellite estimates of wind speed and latent heat flux over the global oceans, *J. Clim.*, 16, 637–656, doi:10.1175/1520-0442(2003)016<0637:SEOWSA>2.0.CO;2.

Bosilovich, M., F. Robertson, and J. Chen (2009), NASA's Modern Era Retrospective-analysis for Research and Applications (MERRA): Global Energy and Water Budgets, *Sixth International Scientific Conference on the Global Energy and Water Cycle*, Melbourne Australia.

Bjerknes, J. and H. Solberg (1922), Life cycle of cyclones and the polar front theory of atmospheric circulation, Geofys. Publ., 3, 1–18.

Bourassa, M. A. (2006), Satellite-based observations of surface turbulent stress during severe weather, *Atmosphere - ocean interactions*, *Vol 2*., W. Perrie, 35-52.

—, M. A. (2004), An improved sea state dependency for surface stress derived from in situ and remotely sensed winds, *Advances in Space Res.*, 33, 1136-1142.

—, M. A., D. G. Vincent, W. L. Wood (1999), A flux parameterization including the effects of capillary waves and sea state, *J*. *Atmos*. *Sci*., 56, 1123-1139.

—, M. A., H. Bonekamp, P. Chang, D. Chelton, J. Courtney, R. Edson, J. Figa, Y. He, H. Hersbach, K. Hilburn, T. Lee, W. T. Liu, D. Long, K. Kelly, R. Knabb, E. Lindstrom, W Perrie, M. Portabella, M. Powell, E. Rodriguez, D. Smith, S. Stoffelen, V. Swail, F. Wentz (2009), Remotely sensed winds and wind stresses for marine forecasting and ocean modeling, *OceanObs '09: Satellite Winds*, 1-23.

—, M. A., S. Gille, C. Bitz, D. Carlson, I. Cerovecki, M. Cronin, W. Drennan, C. Fairall, R. Hoffman, G. Magnusdottir, R. Pinker, I. Renfrew, M. Serreze, K. Speer, L. Talley, G. Wick (2010b), High-Latitude Ocean and Sea Ice Surface Fluxes: Requirements and Challenges for Climate Research, *Bull. Amer. Meteor. Soc.*, (submitted).

—, M. A., S. Gille, D. L. Jackson, J. B. Roberts, and G. A. Wick (2010a), Ocean Winds and Turbulent Air-Sea Fluxes Inferred from Remote Sensing, *Oceanagraphy*, 23, 4, 36-51.

Browning, K.A. (1997), The dry intrusion perspective of extra-tropical cyclone development, *Meteorol. Appl*., 4, 317-324.

—, (2004), The sting at the end of the tail: Damaging winds associated with extratropical cyclones, *Quart. J. Roy. Meteor. Soc.,* 130, 375–400.

Clayson, C. A., C. W. Fairall, and J. A. Curry (1996), Evaluation of turbulent fluxes at the ocean surface using surface renewal theory, *J. Geo. Res.,* 101, doi:10.1029/1996JC02023.

Chelton, D. B., F. J. Wentz (2005), Global Microwave Satellite Observations

Drennan, W. M., J. A. Zhang, J. R. French, C. McCormick, P. G. Black (2010), Turbulent Fluxes in the Hurricane Boundary Layer. Part II: Latent Heat Flux, *J. Atmos. Sci.,* 64 (4), 1103-1115, /doi/abs/10.1175/JAS3889.1.

Evans, J.L. and R.E. Hart (2003), Objective indicators of the life cycle evolution of extratropical transition for Atlantic tropical cyclones, *Mon. Wea. Rev.*, 131, 909-925.

Griffin, J. (2009), Characterization of Errors in Various Moisture Roughness Length Parameterizations, *FSU Pub.*, Tallahassee, Florida: Florida State University.

Hart, R.E., J. L. Evans, and C. Evans (2006), Synoptic composites of the extratropical transition life cycle of North Atlantic tropical cyclones: Factors determining posttransition evolution, *Mon. Wea. Rev.*, 134, 553–578.

Hansen, J., L. Nazarenko, R. Ruedy, M. Sato, J. Willis, A. Del Genio, D. Koch, A. Lacis, K. Lo, S. Menon, et al. (2005), Earth's energy imbalance: Confirmation and implications, *Science,* 308, 1431–1435, doi:10.1126/ science.1110252.

Harr, P. A., and J. M. Dea (2009), Downstream development associated with the extratropical transition of tropical cyclones over the Western North Pacific, *Mon. Wea. Rev.*, 137, 1295–1319.

Jackson, D. L., G. W. Wick, F. R. Robertson (2009), Improved multisensor approach to satellite-retrieved near-surface spcific humidity observations, *J. Geo. Res.,* 114. doi:10.1029/2008JD011341.

Johnson, G.C., J.M. Lyman, J.K. Willis (2007), Global oceans: Heat content, *Bulletin of the American Meteorological Society,* 88, S31–S33.

Kanamitsu, M., W. Ebisuzaki, J. Woollen, S-K Yang, J.J. Hnilo, M. Fiorino, and G. L. Potter (2002), NCEP-DOE AMIP-II Reanalysis (R-2), *Bull. Amer. Meteor. Soc.*, 1631-1643.

Kara, A. B., A. J. Wallcraft, M. A. Bourassa (2008), Air-sea stability effects on the 10 m winds over the global ocean: Evaluations of air-sea flux algorithms, *J. Geophys. Res.*, 113, C04009, doi:10.1029/2007JC004324.

Kent, E. C. and P. K. Taylor (1995), A comparison of sensible and latent heat flux estimates for the North Atlantic Ocean, *J. Phys. Ocean.*, 25, 1530-1549.

Levitus, S., J.I. Antonov, T.P. Boyer, R.A. Locarnini, H.E. Garcia, A.V. Mishonov (2009), Global ocean heat content 1955–2008 in light of recently revealed instrumentation problems, *Geophysical Research Letters,* 36, L07608, doi:10.1029/2008GL037155.

Liu, W. T., and W. Tang (1996), Equivalent neutral wind, JPL Publ., 96– 17, 8 pp.

—, W. T. and X. Xie (2006), Measuring ocean surface wind from space, *Remote Sensing of the Marine Environment, Manual of Remote Sensing, Third Edition, Vol. 6*, J. Gower, Ed., Amer. Soc. For Photogrammetry and Remote Sens., 149-178.

Maue, R. N. (2010), Warm Seclusion Extratopical Cyclones, Dissertation, *FSU Pub.*, Tallahassee, Florida: Florida State University.

Meissner, T. and F. J. Wentz (2002), An updated analysis of the ocean surface wind direction signal in passive microwave brightness temperatures, *IEEE Transactions on Geoscience and Remote Sensing*, 40, 1230-1240.

Neiman, P.J. and M.A. Shapiro (1993), The life cycle of an extratropical marine cyclone: Part I: Frontal-cyclone evolution and thermodynamic air-sea interaction, *Mon. Wea. Rev.*, 121, 2153-2176.

Portabella, M. and A. Stoffelen (2009), On Scatterometer Ocean Stress, *J. Atmos. Oceanic Technol.*, 26, 368-382.

Powell, M. D, P. J. Vickery, T. A. Reinhold (2003), Reduced drag coefficient for high wind speeds in tropical cyclones, *Nature,* 422 (6929), 279-283.

Raymond, D. J. (1992), Nonlinear balance and PV thinking at large Rossby number, *Quart. J. Roy. Meteor. Soc*, 118, 1041–1081.

Roberts, J. B., C. A. Clayson, F. R. Robertson, D. Jackson (2010), Predicting near-surface atmospheric variables from SSM/I using neural networks with a first guess approach, *J. Geo. Res.*, (submitted).

Ross, D. B., V. J. Cardone, J. Overland, R. D. McPherson, W. J. Pierson Jr., and T. Yu (1985), Oceanic surface winds, Adv. Geophys., 27, 101–138.

Rossa, A. M., H. Wernli, and H. C. Davies (2000), Growth and decay of an extratropical cyclone's PV-tower, *Meteorol. Atmos. Phys.*, 73, 139-156.

Saha, S., et al. (2010), The NCEP climate forecast system reanalysis, *Bull. Amer. Meteor. Soc.*, 1015-1057, doi:10.1175/2010BAMS3001.1.

Sanders, F., and J.R. Gyakum (1980), Synoptic-dynamic climatology of the "bomb", *Mon. Wea. Rev.*, 108, 1589-1606.

Schlüssel, P., L. Schanz, and G. Englisch (1995), Retrieval of latent heat flux and longwave irradiance at the sea surface from SSM/I and AVHRR measurements, *Adv. Space Res.*, 16, 107–116, doi:10.1016/0273- 1177(95)00389-V.

Schulz, J., P. Schlu¨ssel, and J. Grassl (1993), Water vapour in the atmo- spheric boundary layer over oceans from SSM/I measurements, *Int. J. Remote Sens.*, 14, 2773–2789, doi:10.1080/01431169308904308.

Shapiro, M. A. and D. A. Keyser (1990), Fronts, jet streams and the tropopause, *Extratropical Cyclones, The Erik Palmén Memorial Volume*, C. W. Newton and E. O. Holopainen, Eds., *Amer. Meteor. Soc.*, 167-191.

Simmons, A., S. Uppala, D. Dee, and S. Kobayashi (2007), The ERA interim reanalysis, *ECMWF Newsletter, No. 110*, ECMWF, Reading, United Kingdom, 25–35.

Smith, S. R., M. Bourassa, J. Rettig, J. Rolph, E. Kent, E. Schulz, R. Verein, S. Rutz, and C. Paver (2009). The data management system for the shipboard automated meteorological and oceanographic system (SAMOS) initiative. *Proceedings of OceanObs'09: Sustained Ocean Observations and Information for Society Conference (Vol. 2)*. Venice, Italy, September 21–25, 2009, J. Hall, D.E. Harrison, and D. Stammer, eds, ESA Publication WPP-306.

Smith, S. R., P. J. Hughes, and M. A. Bourassa (2010), A comparison of nine monthly air-sea flux products, *Int. J. Clim.*, doi: 10.1002/joc.2225.

Weissman, D. E., K. L. Davidson, R. A. Brown, C. A. Friehe, and F. Li (1994), The relationship between the microwave radar cross section and both wind speed and stress: Model function studies using Frontal Air-Sea Interaction Experiment data, *J*. *Geophys*. *Res*., 99, 10087-10108, doi:10.1029/93JC03371.

Weller, R. A., F. Bradley, and R. Lukas (2004), The Interface or Air-Sea Flux Component fo the TOGA Coupled Ocean-Atmosphere Response Experiment and Its Impact on Subsequent Air-Sea Interaction Studies, *J. Atmos. Oceanic Technol.*, 21, 223-257, doi: 10.1175/1520-0426(2004)021<0223:TIOAFC>2.0.CO;2

# BIOGRAPHICAL SKETCH

Joel Scott was born July 28, 1989 in Dallas, Texas. He spent the first half of his childhood in the Dallas Metroplex area, before moving to a ranch in Parker, Colorado at the age of eight. Life near the Rocky Mountain range began to shape Joel's interest in the weather, living through snowstorms and hearing meteorological terms such as downsloping. As a native Texan, Joel could not stay away from his roots for long. He moved back, this time landing in Austin, Texas. While living in the Texas Hill Country, Joel's interest in meteorology heightened watching the frequent summer thunderstorms pass through the region. Joel graduated high school in May 2006 and went on to attend Texas A&M University, majoring in Meteorology, minoring in Mathematics, and playing volleyball as often as possible. Joel graduated *summa cum laude* with his Bachelor of Science degree in May 2009. He was accepted to graduate school at Florida State University, beginning his graduate studies in August 2009. Joel studied under the co-direction of Dr. Mark Bourassa and Dr. Carol Anne Clayson.